

MAGNETOROTATIONAL INSTABILITY DRIVEN ACCRETION IN PROTOPLANETARY DISKS

XUE-NING BAI

Department of Astrophysical Sciences, Princeton University, Princeton, NJ, 08544

Draft version July 18, 2011

ABSTRACT

Non-ideal MHD effects play an important role in the gas dynamics in protoplanetary disks (PPDs). This paper addresses its influence on the magnetorotational instability (MRI) and angular momentum transport in PPDs using the most up-to-date results from numerical simulations. We perform chemistry calculations using a complex reaction network with standard prescriptions for X-ray and cosmic-ray ionizations. We first show that no matter grains are included or not, the recombination time is at least one order of magnitude less than the orbital time within 5 disk scale heights, justifying the validity of local ionization equilibrium and strong coupling limit in PPDs. The full conductivity tensor at different disk radii and heights is evaluated, with the MRI active region determined by requiring that (1) the Ohmic Elsasser number Λ be greater than 1; (2) the ratio of gas to magnetic pressure β be greater than $\beta_{\min}(Am)$ as identified in the recent study by Bai & Stone (2011), where Am is the Elsasser number for ambipolar diffusion. With full flexibility as to the magnetic field strength, we provide a general framework for estimating the MRI-driven accretion rate \dot{M} and the magnetic field strength in the MRI-active layer. We find that the MRI-active layer always exists at any disk radius as long as the magnetic field in PPDs is sufficiently weak. However, the optimistically predicted \dot{M} in the inner disk ($r = 1 - 10$ AU) appears insufficient to account for the observed range of accretion rate in PPDs (around $10^{-8} M_{\odot} \text{ yr}^{-1}$) even in the grain-free calculation, and the presence of solar abundance sub-micron grains further reduces \dot{M} by one to two orders of magnitude. Moreover, we find that the predicted \dot{M} increases with radius in the inner disk where accretion is layered, which would lead to runaway mass accumulation if disk accretion is solely driven by the MRI. Our results suggest that stronger sources of ionization, and/or additional mechanisms such as magnetized wind are needed to explain the observed accretion rates in PPDs. In contrast, our predicted \dot{M} is on the order of $10^{-9} M_{\odot} \text{ yr}^{-1}$ in the outer disk, consistent with the observed accretion rates in transitional disks.

Subject headings: accretion, accretion disks — instabilities — magnetohydrodynamics (MHD) — methods: numerical — protoplanetary disks — turbulence

1. INTRODUCTION

Protoplanetary disks (PPDs) around pre-main-sequence stars form from the collapse of protostellar cores as a result of angular momentum conservation (Adams et al. 1987). With a typical lifetime of $1 - 10$ Myrs (e.g., Hillenbrand et al. 1998; Sicilia-Aguilar et al. 2006), PPDs feed gas onto the central protostar, power an outflow and/or jet, and provide the raw materials for the formation of planetary systems. The structure, evolution and dispersal of PPDs are of crucial importance in understanding a wide range of physical problems especially in the area of planet formation (see review by Armitage 2011). As more and more exoplanets are discovered¹, together with the advancement of planet formation theory (e.g., see the book by Armitage (2010), and also see Chiang & Youdin (2010) for a review on planetesimal formation), understanding the gas dynamics in more detail in the PPDs becomes essential.

One of the most important observational constraints relevant to the gas dynamics in PPDs is that PPDs are actively accreting. The accretion signature comes from the UV excess emission that veils the intrinsic

photospheric spectrum of a YSO, which is interpreted as coming from the standing accretion shock formed at the stellar surface (Calvet & Gullbring 1998; Gullbring et al. 2000). More commonly, the accretion rate \dot{M} can be inferred from emission line profiles, in particular the H α line, based on the magnetospheric accretion model (Muzerolle et al. 1998, 2001). The inferred \dot{M} for Classical T-Tauri stars is about $10^{-8 \pm 1} M_{\odot} \text{ yr}^{-1}$ (Hartmann et al. 1998; Calvet et al. 2004; Sicilia-Aguilar et al. 2005), and observations over a wide mass range of protostars reveal a correlation between \dot{M} and the protostellar mass (Muzerolle et al. 2005; Natta et al. 2006; Herczeg & Hillenbrand 2008; Fang et al. 2009). Transitional disks, characterized by optically thin inner holes which may represent a later evolutionary stage of PPDs (Calvet et al. 2002, 2005; Hughes et al. 2007; Espaillat et al. 2007), are also observed to be actively accreting. Although transitional objects are much rarer, the median of their accretion rate from currently available samples is a few times $10^{-9} M_{\odot} \text{ yr}^{-1}$ (Najita et al. 2007; Sicilia-Aguilar et al. 2010). A key question here is, what drives the rapid accretion in PPDs?

The answer may depend on the evolutionary stages of

Electronic address: xbai@astro.princeton.edu

¹ see <http://exoplanet.eu/>

the PPDs, but it appears certain that turbulence plays a crucial role, and evidence of turbulence in PPDs has been reported from sub-millimeter interferometric observations (Hughes et al. 2011). In early phases, the accretion is likely to be primarily driven by the gravitational instability (GI). The GI leads to gravitoturbulence if the cooling rate is less than the orbital frequency, and transports angular momentum outward via non-axisymmetric spiral waves very efficiently (Gammie 2001; Rice et al. 2005). For typical accretion rate in PPDs, and given the opacity dominated by dust grains, gravitoturbulence is likely to be present at intermediate disk radii between a few tens and ~ 100 AU (Vorobyov & Basu 2007; Rafikov 2009; Rice et al. 2010). However, time-dependent calculations of the PPD evolution indicate that after the envelope infall stops ($\lesssim 1$ Myr), the disk is generally not massive enough to sustain the GI (Zhu et al. 2010). Other driving mechanisms at the inner disk as well as beyond the infall (embedded) phase are clearly needed.

The most important mechanism for driving accretion in non-self-gravitating thin disks is believed to be the magnetorotational instability (MRI, Balbus & Hawley 1991), which generates turbulence and efficiently transports angular momentum radially outward (Hawley et al. 1995; Stone et al. 1996). The MRI requires sufficient coupling between the gas and the magnetic field. However, PPDs are only weakly ionized. The main ionization sources such as cosmic rays and X-rays from the protostar only effectively ionize the surface layer of the disk, making the surface layers “active” to MRI driven turbulence, while the gas in the midplane remains poorly coupled to the magnetic field and is termed “dead” (Gammie 1996). The layered accretion scenario has been studied in great detail via both numerical calculations in a fixed disk model with a chemical reaction network (Sano et al. 2000; Fromang et al. 2002; Semenov et al. 2004; Ilgner & Nelson 2006; Bai & Goodman 2009; Turner & Drake 2009), and MHD simulations (Fleming & Stone 2003; Turner et al. 2007; Turner & Sano 2008; Ilgner & Nelson 2008; Oishi & Mac Low 2009). These research works generally confirm that a “dead zone” is expected at the inner part of the PPDs (about $0.5 - 10$ AU), though its radial and vertical extent depends on the ionization rate and the abundance of small (sub-micron) dust grains.

Because of the low ionization level in PPDs, the gas dynamics is controlled by a number of non-ideal MHD effects, including Ohmic resistivity, Hall effect and ambipolar diffusion (see Balbus (2011) for a review). All calculations and simulations mentioned above considered only the effect of Ohmic resistivity. However, Hall effect and ambipolar diffusion (AD) also play an important role, and dominate Ohmic resistivity in the more tenuous and more strongly magnetized disk upper layers (Salmeron & Wardle 2005, 2008; Wardle 2007). The linear dispersion properties of the MRI in the Hall and AD regimes differ substantially from those in the Ohmic regime. In particular, the inclusion of the Hall effect makes the properties of the MRI depend on the orientation of the magnetic field (Wardle 1999; Balbus & Terquem 2001; Wardle & Salmeron 2011). In the presence of both vertical and azimuthal field, MRI

can grow at appreciable rate even in the limit of infinitely strong AD (Kunz & Balbus 2004; Desch 2004).

The effects of Ohmic, Hall and AD on the non-linear evolution of the MRI have been studied separately by various numerical simulations. One of the key questions addressed by these simulations is that under which conditions can the MRI be sustained. It has been found that for Ohmic resistivity, MRI can be sustained when the vertical Elsasser number $\Lambda_z \equiv v_{Az}^2/\eta_O\Omega$ is greater than unity (Turner et al. 2007; Ilgner & Nelson 2008), where v_{Az} is the vertical component of the Alfvén velocity, η_O is the Ohmic resistivity, and Ω is the angular frequency of the disk. Numerical simulations including both the Ohmic resistivity and the Hall term were performed by Sano & Stone (2002a,b). They found that the Hall effect does not strongly affect the saturation level of the MRI, and the $\Lambda_z > 1$ criterion for the MRI to be sustained still holds with the inclusion of the Hall term. Although their exploration of the Hall parameter was not quite complete (Wardle & Salmeron 2011), these results are not surprising given the fact that the Hall term is not dissipative.

In our recent paper, Bai & Stone (2011) (hereafter, BS11), we studied the effect of AD on the non-linear evolution of the MRI in the strong coupling limit, which applies when the ion inertia is negligible and the recombination time is much shorter than the orbital time. This assumption will be justified in this paper in the context of PPDs. The effect of AD is characterized by the Elsasser number based on AD, denoted by Am , which describes the number of times a neutral molecule “collides” (i.e., exchanges much of its momentum) with the ions in an orbital time. The key result of BS11 is summarized in their Figure 16: MRI can be sustained at any value of Am , provided that the magnetic field is sufficiently weak $\beta \geq \beta_{\min}(Am)$, where β is the ratio of gas to magnetic pressure (see Equation (25) of BS11), and $\beta_{\min}(Am)$ increases with decreasing Am . This relation provides another constraint on the sustainability of the MRI.

In this paper, we aim at studying the location and extent of the active regions in PPDs, and predicting the MRI-driven accretion rate in the most realistic manner by incorporating all the currently available numerical simulation results. We do so by solving a complex set of chemical reaction network established in Bai & Goodman (2009) (hereafter BG09). A single population of dust grains is also included in the network. Magnetic diffusion coefficients are calculated from the equilibrium abundance of charged species. A unique feature in our treatment is that we have included the full dependence of magnetic diffusion coefficients (hence the Elsasser number) on the magnetic field strength, with the field strength constrained by the results from non-ideal MHD simulations. This allows us to predict the magnetic field strength and the accretion rate in PPDs using the least amount of assumptions. One closely related work is by Wardle (2007), who performed similar chemistry calculations to obtain magnetic diffusivities of all non-ideal MHD effects with a simpler reaction network, but the extent of the active layer and accretion rate was not addressed in detail which may be partly due to the unavailability of numerical simulation results. Another closely related work to ours is by Perez-Becker & Chiang

(2011a), who were motivated by the accretion problem in transitional disks and the role of tiny grains. They have considered both Ohmic resistivity and AD, although their adopted criteria were more simplified and did not account for the role of magnetic field strength.

This paper is structured as follows. We begin by reviewing the derivation of various non-ideal MHD effects in Section 2. We describe our chemical reaction network and calculation of magnetic diffusivities in Section 3, where we also discuss our adopted criteria for the MRI-active layer. In Section 4 we present the results of our fiducial model calculation, where a framework for estimating the accretion rate and the magnetic field strength is provided. Using this framework, we study the dependence of accretion rate on various ionization and disk model parameters in Section 5. We summarize and conclude in Section 6.

2. OVERVIEW OF NON-IDEAL MHD EFFECTS

Non-ideal MHD effects derive from the generalized Ohm's law. In the single-fluid framework for weakly ionized gas, fluid density ρ and velocity \mathbf{v} specify the density and velocity of the neutrals. Let charged species j has particle mass m_j , charge $Z_j e$, number density n_j , and drift velocity relative to the neutrals \mathbf{v}_j . Charge neutrality condition applies for non-relativistic MHD: $\sum_j n_j Z_j = 0$ (note that Z_j can be either positive or negative). Let \mathbf{E}' be the electric field in the frame co-moving with the neutrals, while for non-relativistic MHD, the magnetic field \mathbf{B} is the same in all frames. In this co-moving frame, the equation of motion for charged species (whose inertia is negligible) is set by the balance between the Lorentz force and the neutral drag, given by

$$Z_j e (\mathbf{E}' + \frac{\mathbf{v}_j}{c} \times \mathbf{B}) = \gamma_j \rho m_j \mathbf{v}_j, \quad (1)$$

where $\gamma_j \equiv \langle \sigma v \rangle_j / (m + m_j)$ with $\langle \sigma v \rangle_j$ being the rate coefficient for momentum transfer between charged species j and the neutrals, and m is the averaged particle mass of the neutrals.

The relative importance between the Lorentz force and the neutral drag is characterized by the ratio between the gyrofrequency and the momentum exchange rate

$$\beta_j \equiv \frac{Z_j e B}{m_j c} \frac{1}{\gamma_j \rho}. \quad (2)$$

Charged species j is strongly coupled with neutrals if $|\beta_j| \ll 1$, and is strongly tied to magnetic fields when $|\beta_j| \gg 1$.

Since the current density is given by $\mathbf{J} = e \sum_j n_j Z_j \mathbf{v}_j$. The generalized Ohm's law can be obtained by inverting equation (1) to express \mathbf{v}_j as a function of \mathbf{E}' . The result is

$$\mathbf{J} = \sigma_O \mathbf{E}'_{\parallel} + \sigma_H \hat{\mathbf{B}} \times \mathbf{E}'_{\perp} + \sigma_P \mathbf{E}'_{\perp}, \quad (3)$$

where subscripts \parallel and \perp denote vector components parallel and perpendicular to the magnetic field \mathbf{B} , and $\hat{\mathbf{B}}$ denotes unit vector. The Ohmic, Hall and Pedersen con-

ductivities are (Wardle 2007)

$$\begin{aligned} \sigma_O &= \frac{ec}{B} \sum_j n_j Z_j \beta_j, \\ \sigma_H &= \frac{ec}{B} \sum_j \frac{n_j Z_j}{1 + \beta_j^2}, \\ \sigma_P &= \frac{ec}{B} \sum_j \frac{n_j Z_j \beta_j}{1 + \beta_j^2} \end{aligned} \quad (4)$$

respectively. Note that the Hall conductivity depends on the sign of Z_j , while σ_O and σ_P are always positive since β_j has the same sign as Z_j .

The Ohm's law (3) can be inverted to give the electric field using current densities, which then leads to the induction equation modified by non-ideal MHD terms

$$\frac{\partial \mathbf{B}}{\partial t} = \nabla \times (\mathbf{v} \times \mathbf{B}) - \frac{4\pi}{c} \nabla \times [\eta_O \mathbf{J} + \eta_H (\mathbf{J} \times \hat{\mathbf{B}}) + \eta_A \mathbf{J}_{\perp}], \quad (5)$$

where

$$\begin{aligned} \eta_O &= \frac{c^2}{4\pi\sigma_O}, \\ \eta_H &= \frac{c^2}{4\pi\sigma_{\perp}} \frac{\sigma_H}{\sigma_{\perp}}, \\ \eta_A &= \frac{c^2}{4\pi\sigma_{\perp}} \frac{\sigma_P}{\sigma_{\perp}} - \eta_O, \end{aligned} \quad (6)$$

are the desired Ohmic, Hall and ambipolar diffusivities as in equation (5), determined by the microphysics of ion-neutral and electron-neutral collisions, and $\sigma_{\perp} \equiv \sqrt{\sigma_H^2 + \sigma_P^2}$. Note that only η_O is independent of B . The absolute value of these diffusion coefficients determines the relative importance of the Ohmic, Hall and AD terms.

The most commonly used magnetic diffusivities are obtained by assuming that electrons and positively charged ions are the only charge carriers, with all ions having the same Hall parameter. In this case, one can express the conductivities in terms of β_e and β_i for electrons and ions respectively, and since $|\beta_e| \gg \beta_i$, one finds (Salmeron & Wardle 2003)

$$\frac{\partial \mathbf{B}}{\partial t} = \nabla \times (\mathbf{v} \times \mathbf{B}) - \nabla \times \left[\frac{4\pi\eta_e}{c} \mathbf{J} + \frac{\mathbf{J} \times \mathbf{B}}{en_e} - \frac{(\mathbf{J} \times \mathbf{B}) \times \mathbf{B}}{c\gamma_i \rho \beta_i} \right]. \quad (7)$$

Physically, because the electrons are the most mobile species in the gas, the magnetic field is effectively carried by the electrons. Correspondingly, the Hall and AD terms originate from electron-ion drift and ion-neutral drift respectively. In dense regions with weak magnetic field, both electrons and ions are well coupled to the neutrals ($1 \gg |\beta_e| \gg \beta_i$), and Ohmic resistivity dominates. In tenuous regions with strong magnetic field, both electrons and ions are tied to the magnetic field ($|\beta_e| \gg \beta_i \gg 1$), and AD dominates due to the ion-neutral drift. The Hall dominated regime due to the electron-ion drift lies in between, where electrons are tied to the magnetic field while the ions are coupled to the neutrals ($|\beta_e| \gg 1 \gg \beta_i$). The above formula no longer holds when a substantial fraction of charged particles are

grains (Bai 2011), although it is widely used for its simplicity and physical clarity. In this paper, we shall adopt the general expression for magnetic diffusivities (6).

The energy dissipation rate associated with the non-ideal MHD effects is given by

$$\dot{E} = \frac{1}{c} \mathcal{E}_n \cdot \mathbf{J} = \frac{4\pi}{c^2} (\eta_O J^2 + \eta_A J_\perp^2), \quad (8)$$

where $\mathcal{E}_n \equiv (4\pi/c)[\eta_O \mathbf{J} + \eta_H(\mathbf{J} \times \hat{\mathbf{B}}) + \eta_A \mathbf{J}_\perp]$ is the electromotive force associated with the non-ideal MHD terms. We see that the Ohmic resistivity dissipates the total current (leading to magnetic reconnection), while AD damps the perpendicular component of the current (via ion-neutral drag). On the other hand, the Hall effect is not dissipative. It describes the magnetic diffusion due to drift motion between charged carriers without breaking magnetic field lines, and is also present in fully ionized plasma.

3. CALCULATIONS OF NON-IDEAL MHD EFFECTS IN PPDs

As discussed in Section 2, full assessment of the non-ideal MHD effects requires knowledge of the number densities of all charged species in PPDs. In this section, we describe our chemistry calculations to infer magnetic diffusivities in PPDs and provide a quantitative criterion for judging whether the MRI can operate or not under the given diffusivities based on results from numerical simulations. Most of the chemistry calculation procedures are adopted from BG09.

3.1. Disk Model

Fiducially, we take the minimum-mass solar nebula (MMSN) model (Weidenschilling 1977; Hayashi 1981) as our disk model, which is simply constructed by smearing the required mass for forming the solar system planets into a smooth distribution. It represents the minimum amount of disk mass required for forming the solar system planets. The surface mass density and disk temperature are given by

$$\begin{aligned} \Sigma_g &= 1700 r_{\text{AU}}^{-3/2} \text{ g cm}^{-2}, \\ T &= 280 r_{\text{AU}}^{-1/2} \text{ K}, \end{aligned} \quad (9)$$

where r_{AU} is the disk radius measured in AU, and the disk is treated as vertically isothermal. By default, we assume the mass of the protostar to be $M_* = 1M_\odot$, with the Keplerian frequency $\Omega = \sqrt{GM_*/r^3}$. The mean molecular weight of the neutrals is taken to be $\mu_n = 2.34m_H$, from which the sound speed $c_s = \sqrt{kT/\mu_n m_p}$ and disk scale height $H = c_s/\Omega$ can be found.

In addition, we also consider the solar nebula model proposed by Desch (2007), which takes into account the recent advances in the planet formation theory (in particular, the “Nice” model, Tsiganis et al. 2005), and is much more massive than the MMSN. The surface density and temperature profiles are given by

$$\begin{aligned} \Sigma_g &= 5 \times 10^4 r_{\text{AU}}^{-2.17} \text{ g cm}^{-2}, \\ T &= 150 r_{\text{AU}}^{-0.43} \text{ K}, \end{aligned} \quad (10)$$

where the temperature profile is estimated from Chiang & Goldreich (1997).

Submillimeter interferometric observations of the ~ 1 Myr old Ophiuchus star forming regions by Andrews et al. (2009, 2010) have revealed the density and temperature profiles in the outer regions ($\gtrsim 10$ AU, due to limited spatial resolution) for a sample of PPDs. The surface density for the majority of the disks appears to match the MMSN value well at 10–20 AU. Although the fitted density profile in the outer disk is shallower than the MMSN and the Desch’s model (with the median slope of -0.9 rather than -1.5 or -2.2), the surface density profile of the inner disk is not well constrained by observations, and both MMSN and the Desch’s model may be viable choices. Furthermore, global calculations of PPD evolution do indicate much higher surface mass densities in the inner disk than direct continuation of the observed density profiles to small radii (Zhu et al. 2010).

3.2. Ionization Sources

The PPDs are generally too cold for thermal ionization to take place except in the innermost regions (< 1 AU, Fromang et al. 2002). We are interested in regions with $r \gtrsim 1$ AU and consider the following three non-thermal ionization sources.

First, the X-ray ionization from the protostar. Most T-Tauri stars produce strong X-ray emission due to corona activities (see review by Feigelson et al. 2007). The X-ray fluxes are generally variable, with large X-ray flares recurring on time scale of a few weeks (Stelzer et al. 2007). The X-ray emission during the flares is harder than that in the quiescent state. The time averaged X-ray luminosity is roughly proportional to stellar mass, and is about 10^{29} to 10^{31} erg s $^{-1}$ for solar mass stars (Preibisch et al. 2005; Güdel et al. 2007), with typical X-ray temperature ranging from 1–8 keV (Wolk et al. 2005). We adopt the X-ray temperature $T_X = 5$ keV, and X-ray luminosity $L_X = 10^{30}$ erg s $^{-1}$ as our standard model parameters. We take the ionization rate (ξ_X^{eff}) calculated by Igea & Glassgold (1999), which takes into account both absorption and scattering of X-ray photons. In practice, we use the fitting formula given by BG09 (see their Equation (21))

$$\begin{aligned} \xi_X^{\text{eff}} &= \frac{L_{X,30}}{r_{\text{AU}}^{2.2}} \left[4.0 \times 10^{-11} e^{-(N_H/N_1)^{0.5}} \right. \\ &\quad \left. + 2.0 \times 10^{-14} e^{-(N_H/N_2)^{0.7}} + \text{bot.} \right] \text{ s}^{-1}, \end{aligned} \quad (11)$$

where $L_{X,30} = L_X/10^{30}$ erg s $^{-1}$, $N_1 = 3.0 \times 10^{21}$ cm $^{-2}$, $N_2 = 1.0 \times 10^{24}$ cm $^{-2}$, N_H denotes the column number density of hydrogen nucleus from the point of interest to one side of the disk surface, while the “bot.” symbol represents the dual terms with N_H being the hydrogen column number density to the other side of the disk surface. The column number densities N_1 and N_2 roughly correspond to column mass density of 1.2×10^{-2} g cm $^{-2}$ and 3.9 g cm $^{-2}$ respectively.

Secondly, the cosmic-ray (CR) ionization with ionization rate (Umebayashi & Nakano 1981)²

$$\xi_{\text{CR}}^{\text{eff}} = 1.0 \times 10^{-17} \exp(-\Sigma/96 \text{ g cm}^{-2}) \text{ s}^{-1} + \text{bot.} \quad (12)$$

² See Umebayashi & Nakano (2009) for a more refined formula.

The CR flux is highly uncertain because on the one hand, the flux may be much higher if a supernova explosion occurs in the vicinity of the protostar, and observations of the CR flux toward the diffuse cloud ζ Persei indicate enhanced ionization rate of 10^{-16} s^{-1} (McCall et al. 2003); but on the one hand, the CR flux may be substantially shielded by the stellar wind.

Third, the radioactive decay, primarily the decay of short lived ^{26}Al , produces ionization rate of $3.7 \times 10^{-19} \text{ s}^{-1}$ with half-life 0.717 Myr (Turner & Drake 2009). Here we adopt the ionization rate of 10^{-19} s^{-1} as appropriate for disk ages of around 3 Myr. The radioactive decay is generally too weak to provide sufficient ionization, but it prevents the midplane of the inner disk from being completely neutral.

Other possible ionization sources such as energetic protons from disk and stellar corona (Turner & Drake 2009) are ignored for simplicity. Although the resulting ionization rate may exceed X-ray and cosmic-ray ionization by a factor of as large as 40 (Perez-Becker & Chiang 2011a), their fluxes are highly variable and uncertain. In our calculations we also consider $L_X = 10^{32} \text{ erg s}^{-1}$ whose ionization rate is likely to overwhelm this effect by at least an order of magnitude.

Very recently, Perez-Becker & Chiang (2011b) pointed out another potentially important ionization source: the far ultraviolet (FUV) radiation from the protostar. FUV photons are unattenuated by the hydrogen column, and efficiently ionize tracer species of heavy elements such as C and S with penetration depth of up to 0.1 g cm^{-2} . FUV ionization is not included in our calculation, while its relative importance will be discussed in Sections 4.3 and 5.2.

3.3. Grain Size and Abundance

The abundance and size distribution of grains in PPDs are crucial for disk chemistry. Observationally, they are constrained by modeling the spectra energy distribution (SED) (Chiang & Goldreich 1997; D'Alessio et al. 1998; Dullemond & Dominik 2004). Although the parameters are very degenerate, there have been evidence of grain growth to above micron size (D'Alessio et al. 2001), as well as dust settling (to the midplane, which exhibits as grain depletion, Chiang et al. 2001; D'Alessio et al. 2006; Furlan et al. 2006; Watson et al. 2009). Results from mid-infrared spectroscopy from both T-Tauri stars and Herbig Ae/Be stars (van Boekel et al. 2003, 2005; Przygodda et al. 2003) also revealed the presence of micron-sized grains in a substantial fraction of PPDs. In our chemistry calculation, we adopt a simplified prescription of single-sized, well-mixed grains, and consider grain sizes of $0.1 \mu\text{m}$ and $1 \mu\text{m}$. The internal density of the grains is taken to be 3 g cm^{-3} . Although a size distribution of grains and some level of grain settling would be more realistic, our treatment is sufficient to demonstrate the basic physics. Moreover, BG09 considered two populations of grains and found that the two populations behave essentially independently. They further found that for a range of grain sizes considered ($a = 0.01 \mu\text{m}$ to $1 \mu\text{m}$), the controlling parameter lies somewhere between the total grain surface area, and the grain abundance weighted by linear size. For a population grains with

mass distribution $f(a)$ (with $\int f(a) da = Z = 0.01$), one may conveniently consider

$$S \equiv \int_{a_{\min}}^{a_{\max}} da \left(\frac{a}{1 \mu\text{m}} \right)^{-3/2} \frac{f(a)}{0.01} \quad (13)$$

as a measure of the chemical significance of dust grains. Our choice of $a = 0.1 \mu\text{m}$ and $a = 1 \mu\text{m}$ correspond to $S = 32$ and $S = 1$ respectively. For a continuous size distribution of grains, the situation can be more complicated, but one may calculate the resulting S and use our results as a guide.

Another potentially important ingredient of dust grains is the polycyclic aromatic hydrocarbon (PAH), which represents the smallest end of grain size distribution. More than 50% of the Herbig Ae/Be disks have been detected to have PAH emission (Acke & van den Ancker 2004), while the fraction in T-Tauri stars is much smaller (Geers et al. 2006; Oliveira et al. 2010). The importance of PAHs on the disk conductivity has been raised by Perez-Becker & Chiang (2011a) recently. They argue that PAHs in T-Tauri disks may be equally abundant as in Herbig Ae/Be disks, but they are undetected because T-Tauri stars are much less luminous in ultraviolet (UV) radiation to excite fluorescence emission from the PAHs. The abundance of PAHs in PPDs is not well determined, but the small size of PAHs means that they can have very large abundance (which rapidly recombine electrons) without contributing much to the total dust mass, posing a potential threat to the MRI. In this paper, we do not include PAHs in our chemical network by assuming they are insufficiently abundant. However, in our companion paper (Bai 2011), we point out that due to their own conductivity, charged PAHs can even facilitate the MRI by suppressing the Hall effect and ambipolar diffusion under certain situations.

3.4. Chemical Reaction Network

We adopt the complex chemical reaction network described in full detail in Ilgner & Nelson (2006) and BG09 (see their Section 3). It contains nine elements, 174 gas-phase species and 2083 gas-phase chemical reactions³. The rate coefficients are taken from the UMIST database (Woodall et al. 2007) (except for the ionization reactions, whose rate is given in Table 1 of BG09). We further include a single population of grains as described in the previous subsection. Grain related reactions include collisional charging with electrons and ions, adsorption and desorption of neutrals, and grain collisions. The maximum grain charge is taken to be ± 10 and ± 30 elementary charges for $0.1 \mu\text{m}$ and $1 \mu\text{m}$ grains respectively. This leads to substantial increase of total number of species (to 266 for $a = 0.1 \mu\text{m}$) and total number of reactions (to 4513 for $a = 0.1 \mu\text{m}$ and more than 9000 for $a = 1 \mu\text{m}$) compared with BG. We have made a correction to Ilgner & Nelson (2006) and BG09 in the calculation of the electron sticking coefficient, which is described in Appendix A and discussed in Section 4.1. The calculation

³ We correct the number of gas-phase reactions in BG09 where it was stated to be 2113.

of all other reaction rate coefficients remain unchanged from BG09.

We initialize the chemical reaction network from single-element species, whose abundance is provided in Table 6 of Ilgner & Nelson (2006). For the two metal elements Mg and Fe, we take their abundance relative to hydrogen nucleus to be 1.0×10^{-8} and 2.5×10^{-9} respectively (same as most calculations in BG09). The grains are assumed to be uniformly mixed in the disk with 1% in mass. The large set of stiff ordinary differential equations are evolved by the fourth-order implicit Kaps-Rentrop integrator with adaptive time stepping described in Press et al. (1992). Conservation of charge and elemental abundance is enforced at each step of evolution. The chemical network is evolved for 10^6 years when quasi-equilibrium has reached.

3.5. Calculation of Magnetic Diffusivities

To formally obtain the conductivities one needs to know the momentum transfer rate coefficients $\langle \sigma v \rangle$. For ion-neutral collisions, the neutral atom is induced with an electrostatic dipole moment as it approaches the ions, the resulting rate coefficient is approximately independent of temperature, and is inversely proportional to the reduced mass (Draine (2011), see Table 2.1 and Equation (2.34)):

$$\langle \sigma v \rangle_i = 2.0 \times 10^{-9} \left(\frac{m_H}{\mu} \right)^{1/2} \text{ cm}^3 \text{ s}^{-1}, \quad (14)$$

where $\mu = m_i \mu_n / (m_i + \mu_n)$ is the reduced mass in a typical ion-neutral collision.

For electron-neutral collisions, we adopt the approximate fitting formula from Draine et al. (1983), which applies at $T \gtrsim 100\text{K}$. The dependence of the rate coefficient on T becomes shallower at lower temperatures due to the polarization effects, and we adopt

$$\langle \sigma v \rangle_e = 8.3 \times 10^{-9} \times \max \left[1, \left(\frac{T}{100\text{K}} \right)^{1/2} \right] \text{ cm}^3 \text{ s}^{-1} \quad (15)$$

as an approximation.

For collisions between neutrals and charged grains, the rate coefficient follows equation (14) for sufficiently small grains, while the collision cross section becomes geometric for large grains. Therefore, we have

$$\langle \sigma v \rangle_{gr} = \max \left[1.3 \times 10^{-9} |Z|, 1.6 \times 10^{-7} \left(\frac{a}{1\mu\text{m}} \right)^2 \left(\frac{T}{100\text{K}} \right)^{1/2} \right] \text{ cm}^3 \text{ s}^{-1}. \quad (16)$$

With these collision rate coefficients, it is then straightforward to evaluate the magnetic diffusion coefficients (η_O , η_H and η_A) from equations (2), (4) and (6).

3.6. Recombination Time

The recombination time t_{rcb} is an important quantity for studying the gas dynamics in PPDs. If t_{rcb} is much shorter than the dynamical time (Ω^{-1}), as is required in the so called ‘‘strong coupling’’ limit (Shu 1991), local ionization equilibrium would be a good approximation

and the magnetic diffusion coefficients can be directly evaluated from the ionization rate and local thermodynamic quantities such as density and temperature. This will simplify numerical calculations considerably because a single-fluid approach is sufficient. In the opposite limit, if t_{rcb} is much longer than the dynamical time, a more appropriate approach would be the multi-fluid method.

The recombination time t_{rcb} is not a well-defined quantity when there are multiple species of ions and when grains are present. Here we propose an effective recombination time $t_{\text{rcb}}^{\text{eff}}$ by noticing the fact that resistivity scales linearly with the abundance of ionized species (especially free electrons, see Section 2). After evolving the reaction network to chemical equilibrium, we turn off the ionization sources and let the system relax (recombine) for a short period of time ($\ll 1$ year). We measure the rate of change of the Ohmic resistivity, and the effective recombination time is defined as

$$t_{\text{rcb}}^{\text{eff}} \equiv \frac{\eta_O}{|d\eta_O/dt|}. \quad (17)$$

This definition captures the contribution from all recombination channels and is sensitive to the most rapid recombination processes. It naturally generalizes the recombination time defined for single ion-electron recombination $t_{\text{rcb}}^{\text{sig}} = n_e / (dn_e/dt) \propto 1/n_e$.⁴

3.7. Criteria for Sustaining the MRI

In weakly ionized disks, non-ideal MHD terms dominate the inductive term if the Elsasser number is less than 1, where the Elsasser number based on the Ohmic, Hall and AD terms are defined as

$$\begin{aligned} \Lambda &\equiv \frac{v_A^2}{\eta_O \Omega}, \\ \chi &\equiv \frac{v_A^2}{\eta_H \Omega} \approx \frac{\omega_h}{\Omega}, \\ Am &\equiv \frac{v_A^2}{\eta_A \Omega} \approx \frac{\gamma_i \rho_i}{\Omega}. \end{aligned} \quad (18)$$

Here $v_A = \sqrt{B^2/4\pi\rho}$ is the Alfvén velocity, and the approximate equality in the definition of χ and Am holds in the grain-free case. The Hall frequency $\omega_h \equiv eBn_e/\rho c$ is the cutoff frequency of the left polarized Alfvén waves, which can be rewritten to $\omega_h = (n_e/n)(m_i/\mu_n)\omega_{ci}$ with ω_{ci} being the ion cyclotron frequency, n being the number density of the neutrals, m_i being the ion mass.

Non-ideal MHD effects change the linear properties of the MRI substantially when any of the above Elsasser numbers falls below 1 (Blaes & Balbus 1994; Jin 1996; Wardle 1999; Balbus & Terquem 2001; Kunz & Balbus 2004). Below we summarize numerical studies on the non-linear evolution of the MRI in these non-ideal MHD regimes and provide our criteria on the strength and sustainability of the MRI turbulence, which are crucial to this work.

For the Ohmic resistivity, vertically stratified shearing box simulations have identified that the border between the MRI active and MRI inactive regions is well

⁴ One can also define the effective recombination time based on Hall and ambipolar diffusivities, which gives similar numbers but may have weak dependence on the magnetic field strength.

described by $\Lambda = 1$ (Ilgner & Nelson 2008), or $\Lambda_z = 1$ (Turner et al. 2007), where the vertical Elsasser number $\Lambda_z = v_{Az}^2/\eta_O\Omega$, with v_{Az} being the vertical component of the Alfvén velocity. The former criterion gives slightly thicker active layer since Λ is generally larger than Λ_z by a factor of 3 – 30. The difference between these two criteria can be accommodated by noticing the fact that transition from the MRI active to MRI inactive regions (i.e., the “undead zone”) is relatively smooth, with the extent of the transition region to be about $0.5H$ (Turner & Sano 2008). Therefore, in our calculations, we will simply adopt $\Lambda \gtrsim 1$ as the criterion for the active layer in the Ohmic dominated regime. It provides an optimistic estimate of the lower boundary of the active layer.

For the Hall effect on the MRI, the only existing non-linear study is performed by Sano & Stone (2002a,b). They are motivated by whether the suppression of the MRI by Ohmic resistivity is affected by the Hall effect and performed simulations including both the Ohmic and Hall terms. They found that the saturation level of the MRI is not affected by the Hall effect by much. In particular, the condition for sustained MRI turbulence is still controlled by the Ohmic Elsasser number and appears to be independent of the Hall effect. However, the range of the Hall Elsasser number χ (or $X = 2/\chi$ in their notation) studied by Sano & Stone is relatively narrow. Whether their conclusion can be generalized to the Hall dominated regime is still an open question. In this paper, we tentatively adopt Sano & Stone’s conclusion and ignore the Hall effect on the sustainability of the MRI, but we also discuss the applicability and potential caveat about this simplification in Section 4.2.

The effect of AD on the non-linear evolution of the MRI has been studied by Hawley & Stone (1998) using a two-fluid approach, applicable when the ionization fraction is large and the recombination time is long, and by BS11 when the ion inertia is negligible and when t_{rcb} is much shorter than the orbital period (i.e., the strong coupling limit). The behaviors of the MRI in the two limits differ significantly. As we will show in Section 4.2, the strong coupling limit applies almost everywhere in typical PPDs. In this regime, BS11 showed that the MRI can be self-sustained for any value of Am as long as the magnetic field is sufficiently weak. At a given Am , the maximum magnetic field strength is given by

$$\beta_{\min} = \left[\left(\frac{50}{Am^{1.2}} \right)^2 + \left(\frac{8}{Am^{0.3}} + 1 \right)^2 \right]^{1/2}, \quad (19)$$

where the plasma $\beta = P_{\text{gas}}/P_{\text{mag}}$ is the ratio of gas to magnetic pressure, with $P_{\text{mag}} = B^2/8\pi$. Here β is not to be confused by the Hall parameter for charged particles β_j , which is used only in Section 2.

In sum, our adopted criteria for sustained MRI turbulence is

$$\Lambda \geq 1, \quad \text{and} \quad \beta \geq \beta_{\min}(Am). \quad (20)$$

Besides the potential uncertainty from ignoring the Hall effect, another uncertainty in our adopted criteria is that they are mostly based on unstratified simulations with vertical box size fixed at H (e.g., simulations by Sano & Stone and BS11). Although in the Ohmic

regime unstratified and stratified simulations tend to yield similar criterion (Sano et al. 1998; Fleming et al. 2000; Turner et al. 2007), it is yet to be explored whether the same situation holds for the case of ambipolar diffusion. In addition, above the MRI active layer, magnetic dissipation may generate a hot disk corona, which on the one hand, possesses some stress (although much smaller than that in the active layer, Miller & Stone 2000), and on the other hand, increases β in the upper disk. Despite all these complications, our approach serves as the first step towards more realistic criteria, and moreover, it is sufficiently simple for illustrating our new method for estimating the location of the active layer and the accretion rate in Section 4.3.

3.8. Accretion Rate and Required Field Strength

In the active layer, the MRI generates turbulent stress $T_{r\phi}$ which transports angular momentum outward, and its strength is usually characterized by the α parameter (Shakura & Sunyaev 1973), defined as $T_{r\phi} = \alpha \rho c_s^2$. When MRI is self-sustained, there is a tight correlation between α and the time and volume averaged magnetic energy, which is again characterized by the plasma β (Hawley et al. 1995, BS11)

$$\alpha \approx \frac{1}{2\beta}. \quad (21)$$

Note that this relation holds only in the MRI-active layer.

If accretion in PPDs is solely driven by the MRI in the active layer, a simple relation can be derived connecting the accretion rate \dot{M} to the magnetic field strength (BG09). For steady state accretion, conservation of angular momentum demands

$$\dot{M}\Omega r^2 = 2\pi r^2 \int_{-\infty}^{\infty} dz T_{r\phi} \approx 2\pi r^2 \int_{\text{active}} dz T_{r\phi}, \quad (22)$$

where the last integral is performed across the active layer. Although the dead zone has also been shown to transport angular momentum by non-axisymmetric density waves launched from the active layer (Fleming & Stone 2003; Oishi & Mac Low 2009), which is a generic process in shear turbulence (Heinemann & Papaloizou 2009a,b), its contribution is only a small fraction of that from the active layer, and can be safely ignored. From equation (21), we have $T_{r\phi} = \alpha P_{\text{gas}} \approx P_{\text{mag}}/2$ in the active layer, and the above equation turns to

$$\dot{M} \approx \int_{\text{active}} dz \frac{B^2}{8\Omega}. \quad (23)$$

This is a very useful formula for accretion rate estimation and is quite general for MRI driven angular momentum transport in both ideal MHD or non-ideal MHD regimes. It will be used extensively in Sections 4.3 and Section 5.

In turn, for MRI driven accretion, one can estimate the strength of the magnetic field given the accretion rate. Let the thickness of the active layer be denoted by h_a for each side of the disk, the integral over the vertical height can be replaced by a factor of $2h_a$, which leads to

$$\langle B^2 \rangle \approx 4\dot{M}\Omega/h_a, \quad (24)$$

where the bracket $\langle \cdot \rangle$ means vertical averaging. To obtain a more quantitative estimate of the field strength applicable to PPDs, we consider the MMSN around a $1M_\odot$ protostar. The thickness of the active layer should generally be on the order of the disk scale height $h_a \approx H = c_s/\Omega$, and we obtain

$$\langle B \rangle \approx 2\sqrt{\dot{M}\Omega/H} \approx 1.0\dot{M}_{-8}^{1/2}r_{\text{AU}}^{-11/8} \text{ G}, \quad (25)$$

where $\dot{M}_{-8} = \dot{M}/10^{-8}M_\odot \text{ yr}^{-1}$. We note that in obtaining the above relation, only the temperature profile (to estimate the disk scale height) of the MMSN model is used (which is more reliable than the surface density profile). This relation states that for MRI driven angular momentum transport, strong magnetic field is needed for fast accretion.

For typical accretion rate of $10^{-8}M_\odot \text{ yr}^{-1}$, the implied magnetic field strength is strong, and is in fact close to the equipartition strength for the active layer. Assuming the column density of the active layer Σ_a to be 10 g cm^{-1} (as comparable to the penetration depth of the X-ray ionization), the equipartition field strength is

$$B_{\text{equi}} \approx \sqrt{8\pi} \left(\frac{\Sigma_a}{h_a} c_s^2 \right)^{1/2} \approx 2.3\Sigma_1^{1/2}r_{\text{AU}}^{-7/8} \text{ G}, \quad (26)$$

where $\Sigma_1 = \Sigma_a/10 \text{ g cm}^{-2}$. The simple analysis here shows that to the limiting factor for MRI to drive accretion in PPDs is not only the level of ionization, but also the strength of the magnetic field. A quantitative manifestation of this effect will given in Section 4.3.

4. ACTIVE LAYER IN THE FIDUCIAL MODEL

We refer our fiducial model to the MMSN disk with X-ray luminosity of the protostar being $10^{30} \text{ erg s}^{-1}$ and with cosmic-ray ionizations. Variations to the fiducial model are discussed in the next section. Other parameters are fixed at values specified in the previous section in all calculations.

Using the fiducial model, we run four calculations at two disk radii 1AU and 10AU, with and without grains ($0.1\mu\text{m}$). In each calculation, we evolve the chemical network at fixed radius and scan from the disk midplane up to 5 disk scale heights. At each point, we extract the number density of all species from the end of the evolution (10^6 years) and calculate the magnetic diffusivities as a function of the magnetic field strength. Various aspects of the results are discussed in the following subsections.

4.1. Chemistry

In Figure 1, we show the vertical density profile of various chemical species normalized to the number density of the hydrogen nuclei for calculations at 1 AU. The most important quantity is the ionization fraction $x_e \equiv n_e/n_H$, as plotted in red, which largely determines the strength of the non-ideal MHD effects (Section 2). In addition, we plot the profile of the ionization rate. This figure is to be compared with Figures 3 and 6 in Wardle (2007). It is clear that the ionization fraction is extremely small ($\ll 10^{-6}$ in general), hence the inertia of the charged particles is negligible compared with the

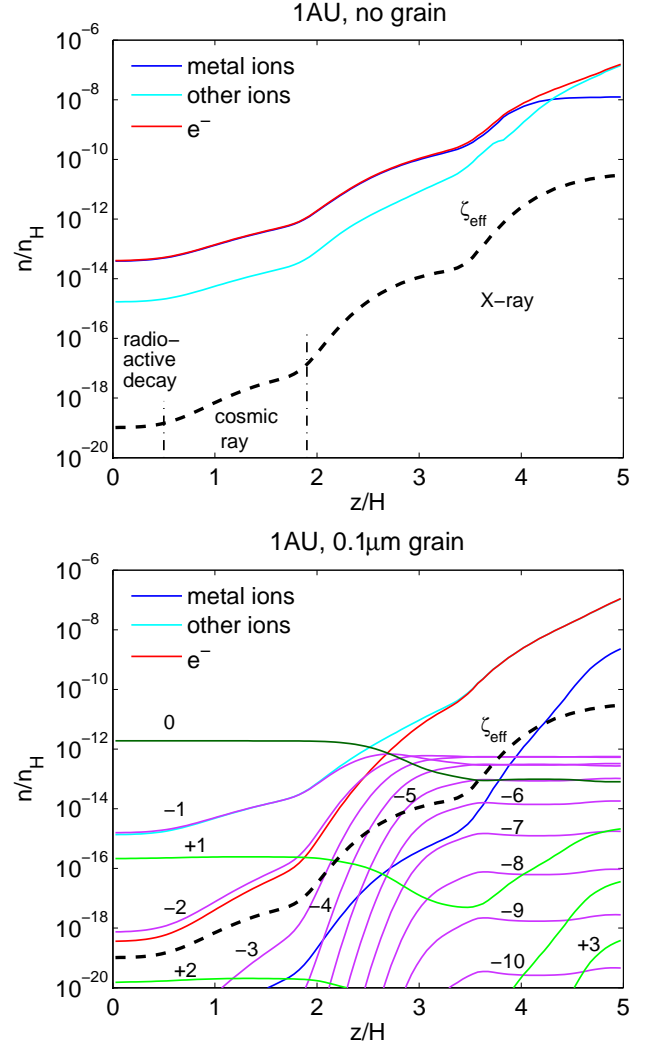


FIG. 1.— Fractional abundance of electrons (red), metal ions (blue) and other ions (cyan) relative to hydrogen nuclei as a function of height (z) above the midplane in our fiducial model at 1AU. Also shown is the ionization rate (bold dashed) as a function of z , divided into three segments where the dominant sources of ionization are labeled. Upper panel: calculation without grains. Lower panel: calculation with well mixed $0.1\mu\text{m}$ grains with 1% in mass. Abundance of positively charged (green), neutral (dark green) and negatively charged (magenta) grains are labeled by their elemental charge Z .

inertia of the neutrals, justifying the first requirement of the strong coupling limit.

The main driving force of chemical evolution is the ionization reactions. In the Figure, there are several “steps” in the vertical profile of the ionization rate that are associated with transitions to different ionization regimes, as described in Section 3.2. These “steps” also make the vertical profile of the ionization fraction x_e exhibit similar features. At the uppermost layer, the ionization rate is the largest and is dominated by direct X-ray ionization from the protostar, with a very small column density of about 0.01 g cm^{-2} . Slightly deeper down, the ionization is still dominated by the X-rays, but is mainly due to the Compton scattered X-ray photons from the upper layer, with penetration depth of about 4 g cm^{-1} . Further

deeper, cosmic-ray ionization with penetration depth of about 100 g cm^{-1} takes over, while around the midplane, radioactive decay dominates. Comparing the result to Figure 2 shown in the next subsection reveals that the ionization rate provided by radioactive decay is generally too small to produce sufficient ionization in PPDs, and can be safely ignored for the purpose of estimating the extent of the active layer and dead zone.

In the grain-free calculation, we see that the ionization fraction primarily overlaps with the metal abundance at $z \lesssim 4H$, indicating that the metals are the dominant electron donor, which has been shown in many previous works (e.g., Fromang et al. 2002; Ilgner & Nelson 2006, BG09). Above $4H$, essentially all the metal atoms are ionized, and the main electron donor is taken over by other ions. The ionization fraction from our calculation differs from that in Wardle (2007) mainly because we use a more complex (and presumably more realistic) chemical network.

The inclusion of well-mixed dust grains with $a = 0.1 \mu\text{m}$ dramatically reduces the ionization fraction. At the midplane, x_e is reduced by 5 orders of magnitude as compared with the grain-free case. The reduction factor is still significant but smaller in the upper layers up to $z \gtrsim 5H$. With grains, the role for metals as the main electron donor is suppressed because the recombination of metal ions is facilitated by grains, consistent with Wardle (2007).

The reduction of electron density by grains has another consequence: when the electron abundance falls substantially below the grain abundance, the ions and grains take over from the electrons to play a decisive role on the conductivity. In the chemistry calculation shown in the bottom panel of Figure 1, this corresponds to regions close to the midplane with $|z| \lesssim 2.5H$. The grain-free formula (7) for magnetic diffusivities no longer holds in this regime: the resistivity η_O is smaller than η_e due to contribution from ions and grains. In addition, Am is no longer independent of magnetic field strength (as can be traced from Figure 3), and becomes larger in stronger field. This effect and its significance is discussed in full detail in Bai (2011).

One difference between our calculation and the calculations by Wardle (2007) is that we have considered the electron sticking probability s_e . This probability s_e was simply taken to be 1 in their calculation. In Perez-Becker & Chiang (2011a), s_e was fixed at 0.1 for PAHs, and 1 for normal grains, while in Okuzumi (2009), s_e was fixed at 0.3 for all grain sizes. However, because electron is much lighter than the grain surface atoms, energy transfer by inelastic collisions with grains is inefficient and the electron may have a large chance to escape. The derivation of electron sticking coefficient with *neutrals* grains has been performed by Nishi et al. (1991), who showed that s_e decreases with increasing temperature, from about 1 at zero temperature to about 1-2 orders of magnitude less than unity at a few hundred K. Ilgner & Nelson (2006) and BG09 adopted this formula in their chemistry calculations, but they erroneously used the same formula for both neutral and charged grains. A generalized derivation of the electron sticking coefficient to include grain charges is given in Appendix A, where

we find that the sticking coefficient for more positively charged grains is progressively smaller than that for negatively charged grains. This is mainly because the electron is accelerated more as it approaches the more positively charged grains, making it more difficult to get rid of the excess energy for adsorption.

The inclusion of the sticking coefficient in grain-electron collisions reduces the electron recombination rate with grains, leading to less dramatic reduction of electron abundance and conductivity. Our test runs indicate that the ionization fraction calculated with and without including the electron sticking probability can differ by up to a factor of 10 in certain regions. The electron sticking probability also affects the grain charge distribution. For example, in Figure 1, the mean grain charge in the disk upper layers from our calculation is about -2.5 elementary charge rather than around -8 in Wardle (2007)'s calculation. Our new result on the charge dependence of s_e implies that grains tend to be (slightly) more positively charged, although this is a relatively weak effect and is more relevant for sub-micron grains.

4.2. Magnetic Diffusivities and Recombination Time

The abundance of all charged species from the chemistry calculation is used to evaluate the magnetic diffusivities using equations (4) and (6), and the results are illustrated in Figure 2. Similar to the figures shown in Wardle (2007), we mark different magnetic diffusion regimes with different filling color. Six magnetic diffusion regimes are considered depending on the relative order among η_O , η_H and η_A . It is clear that Hall and AD becomes more and more important at smaller density (surface layer and large disk radii) and larger magnetic field strength, as expected (η_H scales as B/n_e while η_A scales as B^2/n_e). The addition of grains dramatically changes the pattern in the figure at $z \lesssim 3H$, this is because grains carry most of the negative charge instead of electrons (due to the extremely low ionization rate) and the magnetic diffusivity is largely determined by the less mobile ions and grains. In this region, different choices of chemical reaction networks can make a big difference in the resulting magnetic diffusivity pattern. At disk upper layers ($z \gtrsim 3H$), grains play a less important role on the pattern of magnetic diffusivities painted in the Figure since free electrons overwhelms the grains, although the ionization fraction is still affected by the grains.

White vertical lines in Figure 2 show the contours of constant effective recombination time (equation (17)). We see that in all of the four cases, the recombination time is at least one order of magnitude smaller than the dynamical time scale⁵. This result looks counter-intuitive since the recombination time may be expected to be smaller in the disk upper layers due to the low gas density. However, this is compensated by the enhanced electron abundance near the disk surface (as $t_{rc} \sim 1/nx_e$). Together with the extremely low ionization

⁵ Note that our definition of t_{rcb}^{eff} in equation (17) captures the most rapid recombination process. It is typically shorter than the chemical equilibrium time estimated in Perez-Becker & Chiang (2011a), which is sensitive to the slowest chemical processes

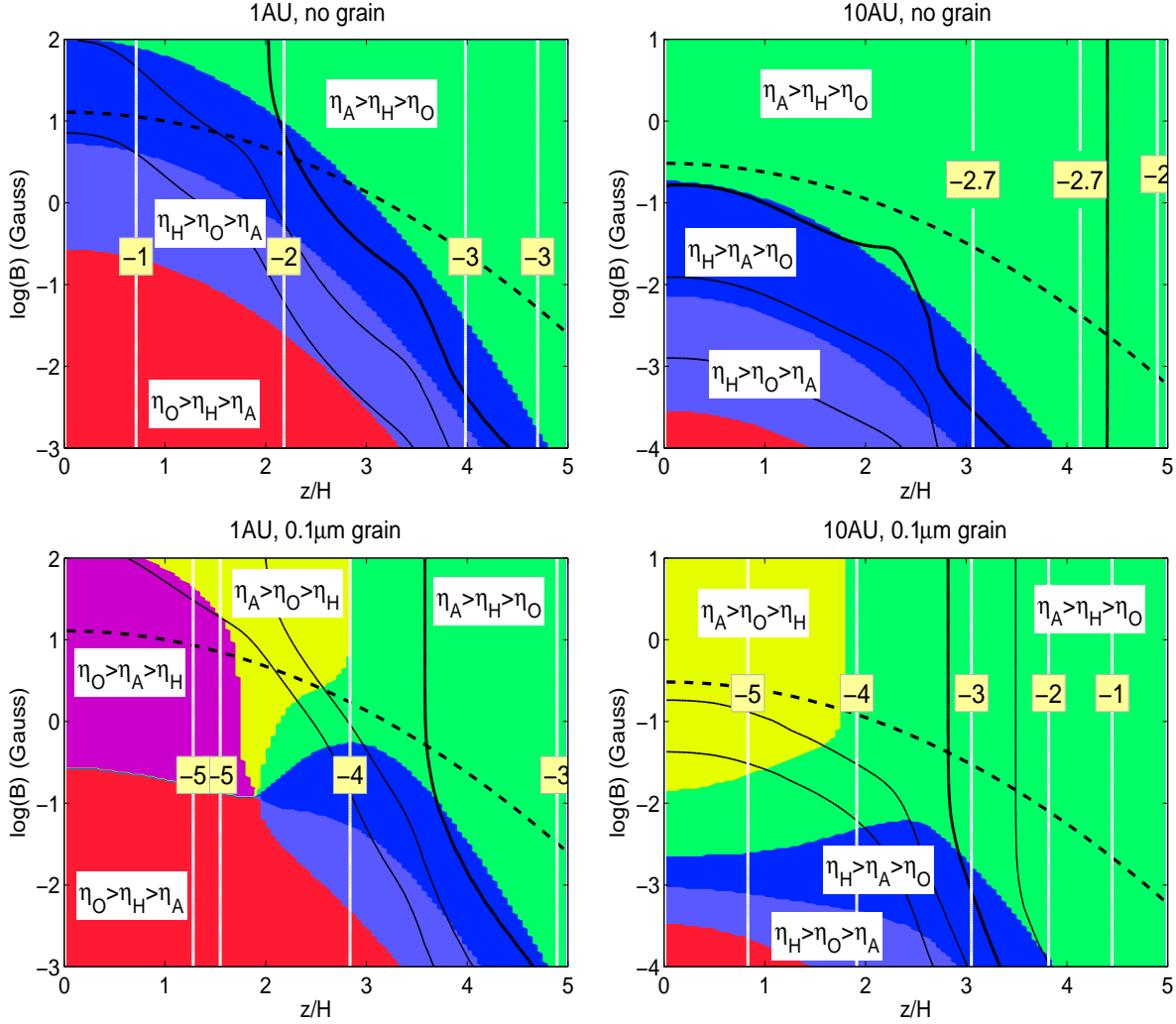


FIG. 2.— Regimes of non-ideal MHD effects in fiducial PPD models plotted as contours in the plane of disk height and magnetic field strength. The left (right) two panels correspond to 1 (10) AU of a MMSN model, and the upper (lower) two panels correspond to the case without grains (with 1% of well mixed $0.1\mu\text{m}$ grain). Different regimes of non-ideal MHD effects are painted with different background colors. *Red and magenta*: Ohmic resistivity dominated; *Dark and light blue*: Hall effect dominated; *Green and yellow*: AD dominated. Subdivisions of the color scheme are indicated in the plots. *Black contours* show constants of the Elsasser number Λ_{tot} which is increased by factors of 10 from bottom left to upper right, with the $\Lambda_{\text{tot}} = 1$ contour marked in bold. The *bold dashed black line* indicates where the magnetic pressure equals to the gas pressure ($\beta = 1$). White *vertical lines* correspond to contours of constant effective recombination time $t_{\text{rcb}}^{\text{eff}}$, labeled by $\log_{10}(\Omega t_{\text{rcb}}^{\text{eff}})$.

level in PPDs, this result demonstrates that the strong coupling limit applies in essentially most regions of typical PPDs, and it justifies that single fluid treatment of the gas dynamics in PPDs is generally sufficient. In particular, the single fluid simulations by BS11 on the effect of AD on the MRI is directly relevant to PPDs, while two-fluid simulations by Hawley & Stone (1998) are not quite applicable.

Moreover, we emphasize that our conclusion that $\Omega t_{\text{rcb}}^{\text{eff}} \ll 1$ is obtained by using the complex chemical network. The usage of a simple network such as the Oppenheimer & Dalgarno (1974) model can lead to different conclusions: At 1 AU without grains, we find that t_{rcb} is about one order of magnitude longer when calculated with the simple network, and becomes longer than the dynamical time at $|z| \lesssim H$. This is because of the lack of recombination channels in the sim-

ple network, and is relevant to the “revival” of the dead zone by turbulent mixing of free electrons from the active layer to the midplane, as seen in multi-fluid simulations with a co-evolving simple chemical reaction network (Turner et al. 2007; Turner & Sano 2008; Ilgner & Nelson 2008). However, with a more realistic chemical network, the reactivation of the dead zone by turbulent mixing would appear less likely to occur, because the turbulent eddy time is comparable to the dynamical time (Fromang & Papaloizou 2006; Turner et al. 2006; Carballido et al. 2011) and most free electrons would be swallowed by the more rapid recombination process before being mixed down to the midplane. Therefore, the density profile of all charged species in PPDs should be close to local ionization equilibrium, which justifies our adopted criteria in Section 3.7.

In Figure 2, we also plot contours of constant Elsasser

number. Here we define the Elsasser number based on η_{tot} as

$$\Lambda_{\text{tot}} \equiv \frac{v_A^2}{\Omega \eta_{\text{tot}}}, \quad (27)$$

where $\eta_{\text{tot}} = \sqrt{\eta_O^2 + \eta_H^2 + \eta_A^2}$, and it measures the importance of all non-ideal MHD effects as a whole. The Elsasser number is in general larger in upper right and smaller in lower left, with the $\Lambda_{\text{tot}} = 1$ contours plotted in bold black lines. Non-ideal MHD terms dominate the induction term when $\Lambda_{\text{tot}} < 1$, with the properties of the MRI significantly modified. In addition, we plot the contour of $\beta = 1$ in bold dashed line. Before applying our criteria (20), which will be the subject of the next subsection, we note that the bold solid and bold dashed lines may serve as *rough* boundaries enclosing the MRI active region. We see that in all cases the dominant non-ideal MHD processes in these regions are the Hall effect and AD.

As we discussed in Section 3.7, we have ignored the Hall effect on the sustainability of the MRI turbulence. Here we discuss the potential caveats from this simplification. We are most interested in the boundary between MRI active and inactive regions. The lower boundary set by $\Lambda = 1$ is relatively well constrained based on the study of Sano & Stone (2002b), although more numerical study in the Hall dominated regime is still necessary since it is generally the case that $\eta_H > \eta_O$ near the lower boundary. The main uncertainty comes from the upper boundary ($\beta \geq \beta_{\text{min}}(Am)$), which is based on simulations of BS11 that include only AD. From Figure 2, we see that AD is indeed the dominant non-ideal MHD effect close to the line of $\beta = 1$ at 10 AU. Therefore, our criterion $\beta \geq \beta_{\text{min}}(Am)$ should provide a relatively reliable upper boundary on the strength of the magnetic field for MRI to operate. At 1 AU with grains, AD is also likely to be the main limiting factor on the magnetic field strength, while in the grain-free case, the location of the upper boundary is likely to be in the Hall dominated regime, and our criterion may require modification.

4.3. Active Layer and Accretion Rate

Using the profile of magnetic diffusivities in the previous subsection, we estimate the location of the active layer by applying our criteria (20). In Figure 3, we show the $\Lambda = 1$ contour (black bold solid) as well as contours of constant Am (black thin solid) in the z - B plane similar to Figure 2. The former (Ohmic resistivity) controls the lower boundary of the active layer, while its exact location is determined by the strength of the magnetic field: lower for strong field and higher for weak field. This is because the Ohmic Elsasser number $v_A^2/\eta_O\Omega$ is proportional to B^2 , and the disk is better ionized (smaller η_O) in the upper layer. The upper limit on the magnetic field strength characterized by β (blue solid) is controlled by AD, where smaller Am value requires weaker magnetic field. The value of Am above the lower boundary is generally greater than 0.1, and reaches up to 10 in the disk upper layers, which agrees with PAH-free model calculations in Perez-Becker & Chiang (2011a), and the minimum value of β ranges from about 10 to 800. The two constraints combined together give the MRI permitted

region in the z - B plane at a given radius the PPD, as painted in gray.

We see that in all of the four cases, maintaining an MRI active layer is possible if the magnetic field is not too strong. That is, the required field strength to overcome the Ohmic resistivity in the disk upper layer is generally much weaker than the equipartition field. This is partly due to the fact that $\eta_O \propto 1/x_e$ decreases toward the disk surface more rapidly than density (at least for $z < 4H$), making the $\Lambda = 1$ contour steeper than the contours of $\beta = \text{constant}$. Also, Am in the disk upper layer is generally greater than 1, where the required field reduction from equipartition strength is only moderate. The MRI permitted region in the z - B plane shifts to disk upper layers when sub-micron grains are included because of increased η_O . It extends toward the disk midplane as one moves to disk outer regions because the reduction of disk surface density slows the recombination process and allows ionization photons/particles to penetrate deeper. At 10 AU without grains, even the disk midplane becomes active for field strength of a few times 0.01G. These results are all consistent with previous chemistry calculations.

For MRI-driven accretion, the required magnetic field strength at various accretion rates from equation (25) is also shown in Figure 3 (red dashed). We see that in the grain-free calculations, the maximum field strength in the MRI permitted region corresponds to $\dot{M} \approx 10^{-8} M_\odot \text{ yr}^{-1}$, while in the presence of sub-micron grains, the maximum accretion rate is dramatically reduced to well below $10^{-9} M_\odot \text{ yr}^{-1}$. The reduction is mostly due to the retreat of the lower boundary: the $\Lambda = 1$ contour shifts upward, reducing the maximum allowed field strength because of reduced gas pressure; in addition, Am becomes smaller, reducing the allowed field strength further.

We note that most previous calculations either adopt the magnetic Reynolds number $\text{Re}_M \equiv c_s^2/\eta_O\Omega = 100$ as the boundary between the active layer and the dead zone, which implicitly assumes $\beta = 100$ in the entire disk (Fromang et al. 2002; Ilgner & Nelson 2006; BG09; Perez-Becker & Chiang 2011a,b), or adopt the Elsasser number criterion, but assume some constant magnetic field strength (Turner & Drake 2009). From Figure 3, the $\text{Re}_M = 100$ criterion corresponds to using the intersection between the bold solid line ($\Lambda = 1$) and thin blue line ($\beta = 100$) as the boundary. We see that this criterion roughly applies in the grain-free case, but may substantially overestimate the active column when grains are present (i.e., the critical Re_M should be larger than 100). In other words, the reduction of the active layer column density by grains is more serious than previously estimated, complementing our discussion in the previous paragraph.

Our graphical illustration of the maximum accretion rate based on the approximate formula (25) can be improved with a more quantitative calculation to give an absolute upper limit of the accretion rate. This upper limit can be obtained from equation (23), where the integral is performed across the entire disk height that the MRI permitted region extends to, with B chosen to be the maximum value determined by $\beta_{\text{min}}(Am)$. For the

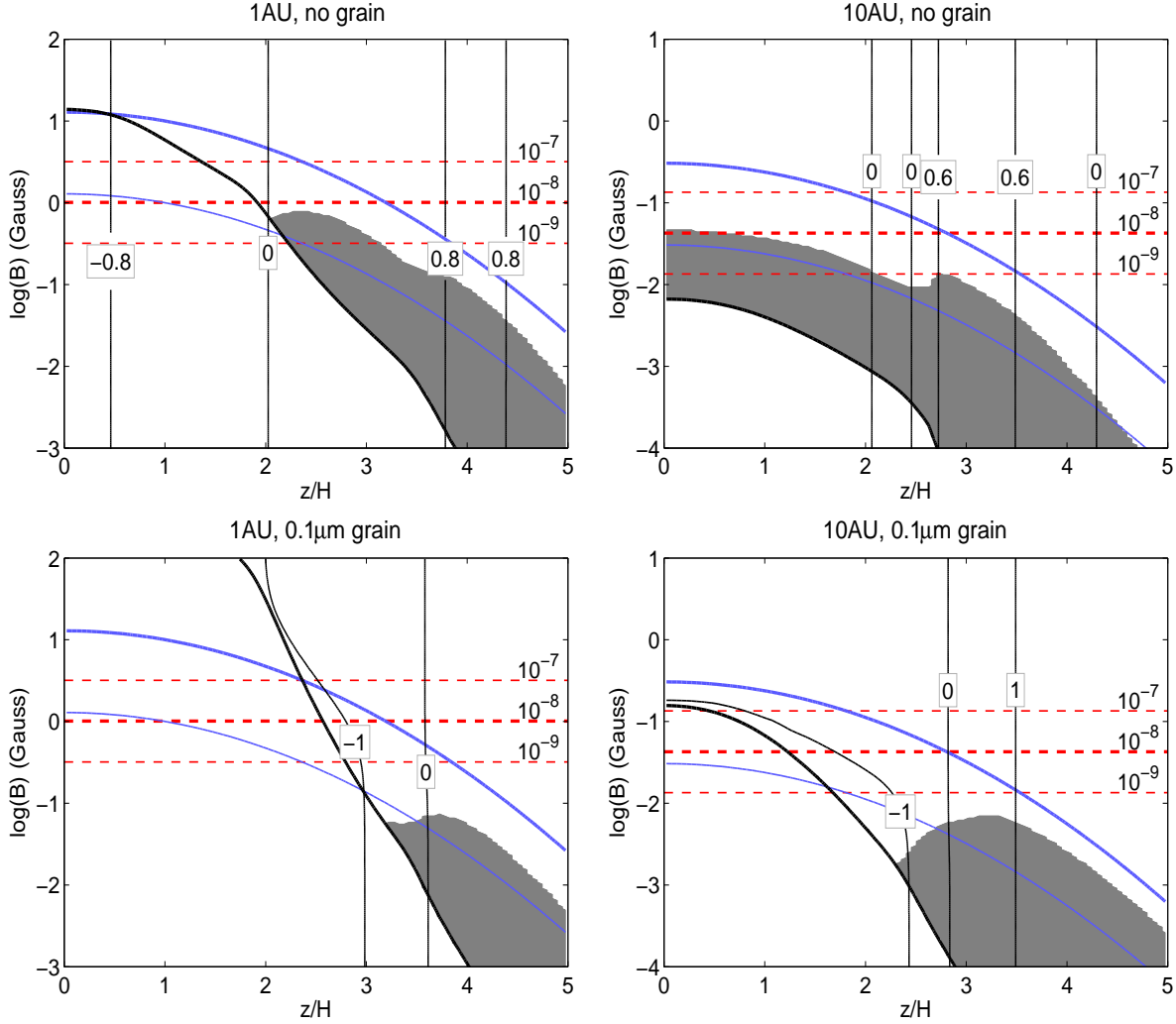


FIG. 3.— Similar to Figure 2, but for constraints on the MRI permitted region in PPDs. The bold solid contours correspond to the Ohmic Elsasser number $\Lambda = 1$, while the thin solid curves show the contours of constant Am labeled by $\log_{10}(Am)$, terminated at $Am = 0.1$. Blue bold and thin lines mark the plasma $\beta = 1$ and $\beta = 100$ respectively. Permitted regions for the MRI in PPDs based on criteria (20) are painted in gray. The red dashed lines indicate the required field strength in the MRI permitted region corresponding to accretion rate of 10^{-7} , 10^{-8} and $10^{-9} M_{\odot} \text{ yr}^{-1}$, respectively, based on equation (25).

MMSN disk model, we have

$$\begin{aligned} \dot{M}_{\max} &\approx \frac{c_s}{8\Omega^2} \int_{\text{active}} B_{\max}^2 \frac{dz}{H} \\ &\approx 0.98 \times 10^{-8} r_{\text{AU}}^{11/4} \int_{\text{active}} \left(\frac{B_{\max}}{G} \right)^2 \frac{dz}{H} M_{\odot} \text{ yr}^{-1}. \end{aligned} \quad (28)$$

For the four calculations in Figure 3, we find the maximum accretion rate (in unit of $M_{\odot} \text{ yr}^{-1}$) to be 4.5×10^{-9} , 1.5×10^{-8} for the grain free model at 1 AU and 10 AU respectively, 3.8×10^{-11} and 2.5×10^{-10} for well-mixed sub-micron grain model at 1 AU and 10 AU. As expected, they agree with the estimate from our graphical illustration.

Our equation (23) provides an convenient way for estimating the accretion rate from the magnetic field strength, but it does not predict a priori the field strength in the disk. Here we consider the following thought experiment and hypothesis from which we pro-

pose a way to predict the strength of the magnetic field in the active layer hence the accretion rate.

Suppose the initial magnetic field strength in the disk is sufficiently weak (say, $\beta = 10^5$ at the disk midplane). According to Figure 3, the MRI first develops in the very upper layer of the disk. The MRI amplifies the magnetic field, and consequently, both the upper and lower boundaries of the active layer moves toward the midplane because of increased field strength⁶. The MRI ultimately saturates into turbulence, and turbulent stirring maintains roughly constant field strength across the active layer (e.g., Oishi & Mac Low 2009). We further hypothesize that the magnetic field in global disks is able to self-organize into a configuration to maximize the

⁶ This is somewhat related to the recurrent growth and decay of the MRI turbulence as a result of field amplification and resistive damping observed by Simon et al. (2011), who adopted a constant resistivity profile. In real situations with a rapidly increasing resistivity toward the disk midplane, the transition may be a more smoothed process.

rate of angular momentum transport by the MRI turbulence. While unjustified due to the lack of systematic global studies (most global simulations of the MRI such as Fromang & Nelson (2006) and local stratified simulations have zero net vertical flux, which leads to relatively weak turbulence), this hypothesis predicts the magnetic field strength and accretion rate that lie on the larger side than in reality (i.e., an optimistic estimate).

Based on the discussion above, we predict the accretion rate as follows. We scan over the strength of the magnetic field B in the active layer (B is assumed to be constant across the active layer), where for each B , we calculate \dot{M} using equation (23). The optimistically predicted accretion rate is the maximum \dot{M} from the scan. For the four calculations in Figure 3, the predicted accretion rates (in unit of $M_\odot \text{ yr}^{-1}$) are 2.7×10^{-9} , 7.7×10^{-9} for grain free models at 1 AU and 10 AU respectively, and 2.3×10^{-11} and 1.3×10^{-10} for well-mixed sub-micron grain models at 1 AU and 10 AU. They are about half the value of the upper limits listed before.

While the framework we just described is fully general, the results reported in this paper are subject to a few caveats due to simplifications in the adopted disk and ionization models that may result in small uncertainties up to a factor of a few. These uncertainties are discussed below and can be overcome by adopting more realistic disk and ionization models that takes into account radiative transfer, thermodynamics and magnetic pressure support to yield more reliable estimate of the accretion rate.

We have assumed constant vertical temperature profile in our estimate of the accretion rate, while in reality, the upper layer of the disk is heated by both the X-ray photons which are responsible for the ionization (Glassgold et al. 2004; Gorti & Hollenbach 2004) and the MRI itself (BG09, Hirose & Turner 2011), raising the temperature above the midplane temperature by a factor of a few. This effect increases the gas pressure, hence plasma β , and allows stronger magnetic field in the active layer, which may lead to higher \dot{M} than our predicted value by a factor of a few.

We have assumed that the gas density profile is Gaussian in our calculations. In reality, magnetic pressure plays more important role in the hydrostatic equilibrium at the disk surface, and local isothermal stratified shearing-box simulations by Miller & Stone (2000) show deviation from Gaussian density profile with gas density at the disk surface a factor of up to 10 higher than our adopted Gaussian model. This may promote accretion by allowing stronger magnetic field near the surface. However, since the ionization rate depends on the column gas density from the disk surface, this effect is compensated by the reduced ionization rate and enhanced recombination rate (at given disk height), giving only order unity corrections to the predicted accretion rate. In fact, the predicted accretion rate does not sensitively depend on the density distribution across disk height, and the approximate calculations by Perez-Becker & Chiang (2011b) that are free from the vertical density distribution are generally consistent with ours within order unity.

Simulations by Miller & Stone (2000) also indicates

non-zero stress in the magnetic corona, but the α value is generally one order of magnitude smaller than that in the disk. The coronal contribution to the accretion rate is about $\alpha P_c h_c$, with the coronal gas pressure P_c orders of magnitude smaller than that in the disk midplane / active layer, and the coronal thickness h_c on the order of a few disk scale height (not much thicker than that of the active layer). Therefore, for our purpose, accretion in the magnetic dominated disk corona can be safely neglected.

Recently, Perez-Becker & Chiang (2011b) called for attention to the role of the FUV ionization, which produces much higher ionization fraction than other ionization sources (making $Am \gtrsim 1000$) with penetration depth of about $0.01 \text{ g cm}^{-2} \lesssim \Sigma_{FUV} \lesssim 0.1 \text{ g cm}^{-2}$. We note that in the MMSN model, 0.1 g cm^{-2} corresponds to $z \approx 3.8H$ at 1 AU and $z \approx 2.9H$ at 10 AU, which are very upper layers in the disks. Comparing with Figure 3 we see that at such heights, the equipartition field strengths in the active layer correspond to \dot{M} of a few times $10^{-10} M_\odot \text{ yr}^{-1}$ and a few times $10^{-9} M_\odot \text{ yr}^{-1}$ respectively, which set the upper limit for the MRI accretion rate driven by FUV ionization. The upper limit is a factor of a few below our predicted \dot{M} in the grain-free case, but may well exceed the predicted rate when small grains are included.

In sum, we have provided a general framework for estimating the location of the active layer as well as the accretion rate at a given location of PPDs. The most important feature is that it explicitly incorporates the dependence on the magnetic field strength, with the field strength estimated by our physically motivated hypothesis. Furthermore, the simulation based relation $\alpha = 1/2\beta$ allows us to provide an optimistic estimate as well as a robust upper limit of the accretion rate, without involving additional assumptions about the value of α . This framework will be extensively used for parameter study of the accretion rate in the next section, and can be generalized with more realistic criteria and disk models in the future.

5. PARAMETER STUDY

In this section, we perform a series of chemistry calculations at different disk radii from 1AU to 100AU and explore a number of different model parameters including grain size, ionization rate and disk mass. In each series of the parameter study, we derive the MRI-driven accretion rate \dot{M} as a function of disk radius using the method illustrated in the previous section, in parallel with the predicted magnetic field strength. The results are shown in Figures 4 and 5, with detailed description and discussion given in the subsections that follows. Obviously, using a fixed disk model, the predicted \dot{M} is not necessarily constant as a function of disk radius, which would lead to non-steady accretion if MRI is the only driving mechanism. On the other hand, the predicted spatially varying \dot{M} implies that modifications to the adopted disk model is necessary for steady state accretion. Detailed modeling of the disk structure to match the steady state accretion is beyond the scope of this paper, but the trend can be readily obtained from our studies.

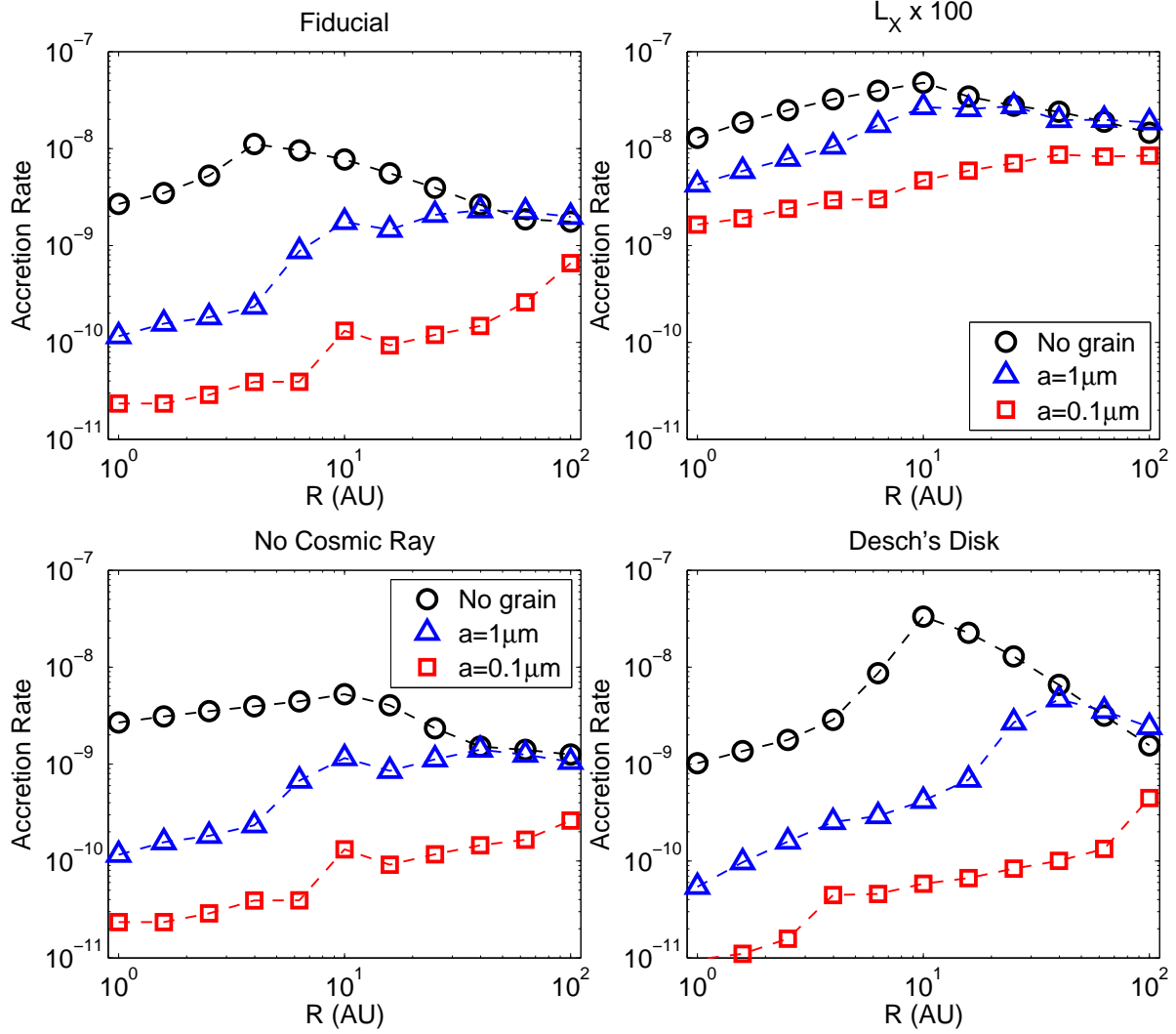


FIG. 4.— The optimistically predicted accretion rate (in unit of $M_\odot \text{ yr}^{-1}$) as a function of disk radius for our fiducial model (upper left): MMSN disk with cosmic ray and X-ray ionization, model with X-ray luminosity 100 times higher (upper right), model without cosmic-ray ionization (lower left) and model with the Desch’s disk (lower right). In each panel, we show results for calculations in the grain-free case (black circles), with well-mixed $1\mu\text{m}$ grains (blue triangles) and with $0.1\mu\text{m}$ grain (red squares).

5.1. The Effect of Grain Size

We begin by considering our fiducial model: MMSN disk with both cosmic ray ionization and X-ray ionization ($L_X = 10^{30} \text{ erg s}^{-1}$). In the upper left panel of Figure 4 we show the predicted \dot{M} as a function of disk radius. We have considered the grain-free case as well as models with $1\mu\text{m}$ and $0.1\mu\text{m}$ well-mixed grains with mass fraction of 1%. Again, we remind the reader that our predicted accretion rate is optimistic.

In general, the predicted \dot{M} increases with disk radius r in the inner disk, and decreases with r in the outer disk. In the former case, the disk midplane is “dead” and accretion is layered. Since $\dot{M} \propto \alpha \Sigma_{\text{active}} T / \Omega$ (where Σ_{active} is the column density of the active layer), assuming both Σ_{active} and α to be constant, one obtains $\dot{M} \propto r$ for the MMSN temperature profile. In reality, as we discussed in Sections 3.7 and 4.3, α is controlled by Am (which is about 1-10 in the active layer), while the thickness of the active layer depends on the mutual effects of Ohmic

resistivity and AD, neither assumptions strictly hold. In Figure 4, we see that the increase of \dot{M} with disk radius in the inner disk is somewhat slower than r .

When the entire disk becomes active, Ohmic resistivity becomes essentially irrelevant in constraining the accretion rate (see the upper right panel of Figures 2 and 3 at $r = 10$ AU for reference). The accretion rate is mainly controlled by the disk surface density, temperature, and the magnetic field strength ($\dot{M} \propto \alpha \Sigma T / \Omega$) through AD. For MMSN, $\Sigma T / \Omega \propto r^{-1/2}$, which gives the main source of accretion rate reduction. The predicted profile of \dot{M} is also affected by the radial profile of the α parameter determined by Am .

In the grain-free calculation, the entire disk becomes active at $r \gtrsim 4$ AU in our fiducial model, and the predicted \dot{M} is between 10^{-9} and $10^{-8} M_\odot \text{ yr}^{-1}$ at all disk radii considered. The reduction of the accretion rate caused by dust grains is substantial. At 1 AU, \dot{M} is reduced by about two orders of magnitude in the pres-

ence of $0.1\mu\text{m}$ grains, while for $1\mu\text{m}$ grains the reduction is more than one order of magnitude. The entire disk becomes active for $r \gtrsim 70$ AU and $r \gtrsim 10$ AU respectively in the above two cases. By and large, the predicted \dot{M} increases with disk radius and flattens out at large radii as discussed before. The rise in predicted \dot{M} in the $0.1\mu\text{m}$ case toward 100 AU is mainly because the cosmic-ray ionization takes over the X-ray ionization (see next subsection).

We find an interesting fact that at very large disk radii ($\gtrsim 40$ AU), calculations with $1\mu\text{m}$ grains lead to comparable or slightly higher \dot{M} than those without grains. By carefully checking the equilibrium abundance of all chemical species, we find that in the grain-free calculations, ionization level near the disk midplane is determined by metal abundance, while the number density of other ions is much smaller (see Figure 1 for example). In the presence of grains, metals are depleted at low temperature (see equation (26) of BG09) due to adsorption onto grain surfaces, and the dominant ion component becomes species such as H_3^+ and HCO^+ (and others) depending on the gas density. The suppression of metals is one of the reasons for the reduction of ionization level, but it appears that at very low density and temperature, slightly higher ionization level can be achieved due to non-metal ions. Nevertheless, we also note that due to uncertainties in the reaction rate coefficients in the UMIST database, the equilibrium abundance of various chemical species such as HCO^+ can be uncertain up to a factor of ~ 4 (Vasyunin et al. 2008).

We see that even in the absence of dust grains, the optimistically predicted \dot{M} is only comparable or below $10^{-8}M_\odot \text{ yr}^{-1}$, which is about the median value of the observed accretion rate in T-Tauri stars (Hartmann et al. 1998; Sicilia-Aguilar et al. 2005). In the presence of dust grains, the accretion rate that can be driven from the MRI is reduced dramatically. The situation is particularly serious for T-Tauri disks, since the gas has to enter through the inner disk to accrete. Given the fact that our choice of parameters are typical, these results pose strong challenge on the effectiveness of the MRI in driving rapid accretion in PPDs. Below we further explore other effects to see whether higher MRI-driven accretion rate can be achieved.

5.2. The Effect of Ionization Rate

Because of the uncertainty in the amount of cosmic-rays, which may be shielded by the stellar winds, we also perform a series of chemistry calculations without cosmic-ray ionization, and the results are shown in the lower left panel of Figure 4. We note that besides deeper penetration depth, the cosmic-ray ionization rate generally exceeds the scattering component of the X-ray ionization rate beyond about 25 AU, and one might expect that cosmic-ray ionization makes significant contributions to our predicted \dot{M} in the outer disk. However, this does not seem to be the case.

In the grain-free case, we find that the transition radius larger than which the entire disk becomes active shifts from about 4 AU in the fiducial model to about 10 AU in the absence of cosmic rays. Nevertheless, the

predicted \dot{M} does not change by much throughout the disk (only slightly reduced). In the presence of grains, the transition radius shifts outward to about 25 AU for the $1\mu\text{m}$ case, and is above 100 AU for the $0.1\mu\text{m}$ case. Again, our predicted \dot{M} is also slightly reduced (generally within a factor of 2) but still similar to the fiducial results. To explain, we note that \dot{M} largely depends on the magnetic field strength in the active layer. Although X-rays do not penetrate as deep as cosmic rays to activate the disk midplane in the outer disk, the permitted magnetic field strength in the active layer turns out to be similar to the case with cosmic rays. According to equation (23), given similar field strength, \dot{M} is then determined by the *geometric* thickness of the active layer, which is on the order of H and is not sensitive to whether the active layer extends to the disk midplane or not.

To examine the role of X-ray ionization, we further consider a model with $L_X = 10^{32} \text{ erg s}^{-1}$, 100 times larger than our fiducial X-ray luminosity. Although such X-ray luminosity is unusually high for T-Tauri stars (Güdel et al. 2007), it provides an upper limit on the accretion rate that can be driven by X-ray ionization. Alternatively, one might also view this unrealistic choice of high X-ray luminosity as an incorporation of other possible but uncertain strong ionization sources such as energetic protons from protostellar activities (Turner & Drake 2009). We see from the upper right panel of Figure 4 that the predicted \dot{M} is much higher than our fiducial model. The rise in \dot{M} is mainly due to deeper penetration in the inner disk ($\lesssim 5$ AU) and due to reduced AD in the outer disk. Accretion rate in grain-free calculations reaches a few times $10^{-8}M_\odot \text{ yr}^{-1}$, which is close to the upper limit of the observed accretion rate. Also, comparing the three curves with their counterparts in the fiducial plot (upper left) indicates that increasing X-ray luminosity is more efficient in raising accretion rate when small grains are present. In sum, it appears that for the MRI to explain the observed rate of accretion in PPDs, much stronger ionization rate than fiducial is needed.

We can also compare our results with the predicted \dot{M} by FUV ionization shown by Perez-Becker & Chiang (2011b)⁷. With the FUV penetration depth of $\lesssim 0.1 \text{ g cm}^{-2}$, they predict \dot{M} of a few times $10^{-10}M_\odot \text{ yr}^{-1}$ at 1 AU and it increases roughly linearly with radius since accretion only proceeds in the upper surface layer with roughly constant surface column density. Comparing with their Figure 5 we see that FUV ionization is likely to be a comparably important ionization source as X-rays (while they drive accretion in different layers), and in the presence of small grains, FUV ionization makes significant contributions to the total MRI-driven accretion rate in the inner disk, and could dominate other ionization sources in the outer disk.

⁷ Two order-unity effects may lead Perez-Becker & Chiang (2011b) to overestimating the accretion rate by a factor of a few compared with ours: (a) Their equation (6) underestimates the density in the disk upper layer by a factor of $\gtrsim 3$ in a Gaussian density profile, thus promoting higher ionization; (b) Their calculations correspond to the maximum possible accretion rate (28), while our predicted rate is about 2 times smaller (see Section 4.3).

5.3. The Effect of Disk Mass

We explore the role of disk mass by repeating our calculations using the Desch’s disk model, while the adopted ionization rates remain fiducial, and the results are shown in the lower right panel of Figure 4. We see that at 1 AU, where the Desch’s disk has about 30 times more surface density than the MMSN disk, the predicted \dot{M} for all three cases (with and without grains) are smaller than the fiducial results. In the grain-free case, the predicted \dot{M} rapidly increases with radius in the inner disk, and peaks at about $r = 10$ AU where the entire disk becomes active. The peak rate exceeds the MMSN model at the same location by a factor of several. The predicted rate falls off towards the outer disk more rapidly than that in the MMSN disk, which is essentially because the surface density of Desch’s disk decreases with radius more rapidly. With the grains, the predicted \dot{M} generally increases with disk radius until saturation (the entire disk becomes active), and the corresponding accretion rate in the outer disk is comparable or slightly exceeds that in the MMSN model. Finally, the rates approach the fiducial results at around 100 AU simply because the surface densities in the two disk models are comparable.

Our results suggest that given the same ionization sources, a more massive disk leads to slower accretion if the accretion is layered, while it is able to sustain faster accretion if the entire disk is active. The reason is that at the same column density from the disk surface (hence the same ionization rate), the gas density is higher in a more massive disk (as one can check with the error function). Therefore, the recombination rate is enhanced, reducing the ionization fraction hence \dot{M} roughly as $\rho^{-1/2}$. On the other hand, higher disk mass in the disk permits stronger magnetic pressure in the active layer, and dominates the former effect when the entire disk column is active.

We have seen that the predicted \dot{M} by the MRI turbulence generally increases with radius in the inner disk, and decreases with radius in the outer disk, with the transition radius depending on the dust content. This result is obviously inconsistent with steady state accretion. Further evolution would lead to pile-up of mass towards the inner disk, with the density profile in the outer disk becoming more flattened. According to the results in this subsection, the pile-up of mass in the inner disk would lead to slower rather than faster accretion, which further enhances the mass pile-up. Therefore, the fact that \dot{M} decreases with disk surface density in the inner disk leads to a runaway pile-up of mass, which may be unsustainable. This result further support the conclusion that mechanisms other than the MRI is needed to drive rapid accretion through the inner disk.

5.4. Predicted Magnetic Field Strength

In Figure 5, we show the (optimistically) predicted magnetic field strength in terms of the ratio of midplane gas pressure to the magnetic pressure in the active layer $\beta_s \equiv P_{\text{mid}}/P_{\text{mag}}$. This is a physically more convenient quantity than the absolute magnetic field strength and provides a guide to numerical modelers. The magnetic

field strength can be obtained by

$$\begin{aligned} B &= 13\beta_s^{-1/2}r_{\text{AU}}^{-13/8} \text{ G} & (\text{MMSN}) \\ B &= 72\beta_s^{-1/2}r_{\text{AU}}^{-1.94} \text{ G} & (\text{Desch}) \end{aligned} \quad (29)$$

Note the steep dependence of the magnetic field strength on disk radius.

Because the active layer resides in the upper disk, with lower gas pressure hence smaller magnetic field, β_s is generally much larger than 1. We see that β_s spans a large range between about 100 and 10^5 , depending on the surface density, ionization rate and disk radius. The predicted field strength is generally stronger (smaller β_s) in the grain-free case since the active layer resides higher in the disk surface in the presence of grains, with lower gas pressure hence smaller magnetic field. The field strength can be raised significantly by strong ionization (upper right panel), accompanied by increased accretion rate as discussed in Section 5.2. For the massive disk model (lower right), β_s in the inner disk is much higher than the fiducial case because the active layer resides at a higher position than in the fiducial model due to the finite ionization penetration depth.

It has been predicted that the presence of ordered magnetic field in PPDs can lead to grain alignment with the magnetic field and produce polarized emission in the millimeter continuum (Cho & Lazarian 2007). Grain alignment is expected in the outer disk, where radiative torque dominates thermal collisions. Recently, however, Hughes et al. (2009) reported non-detection of polarized emission using arcsecond-resolution Submillimeter Array (SMA) polarimetric observations. One suspected reason has to do with the magnetic field strength, which has to be above some critical field strength for the alignment to occur. For $10 - 100\mu\text{m}$ grains, Hughes et al. (2009) calculated the critical field strength to be $10 - 100\text{mG}$ at the location of $50 - 100$ AU (corresponding to the angular resolution of the SMA for the observed sources). However, at such distances, our predicted field strength is less than 2mG (taking $\beta_s = 100$). Therefore, the non-detection of polarized emission is, in fact, consistent with the presence of the MRI, while if polarized emission were detected, the implied magnetic field would be too strong for the MRI to operate in the outer disk.

6. SUMMARY AND DISCUSSION

We have explored the non-ideal MHD effects in protoplanetary disks (PPDs) using chemistry calculations with a complex reaction network including both gas-phase and grain-phase reactions. Cosmic-ray and X-ray ionization processes are included with standard prescriptions. The equilibrium abundance of all charged species are used to calculate the full conductivity tensor, from which diffusion coefficients for Ohmic resistivity, Hall effect and ambipolar diffusion (AD) are evaluated. One major finding from our chemistry calculations is that the recombination time is much shorter than the orbital time in essentially all regions in PPDs, no matter grains are present or not. Together with the extremely low level of ionization in PPDs, this verifies the applicability of the “strong coupling” limit, and the gas dynamics in PPDs can be well described in a single-fluid framework with magnetic diffusion coefficients in non-ideal MHD terms given from

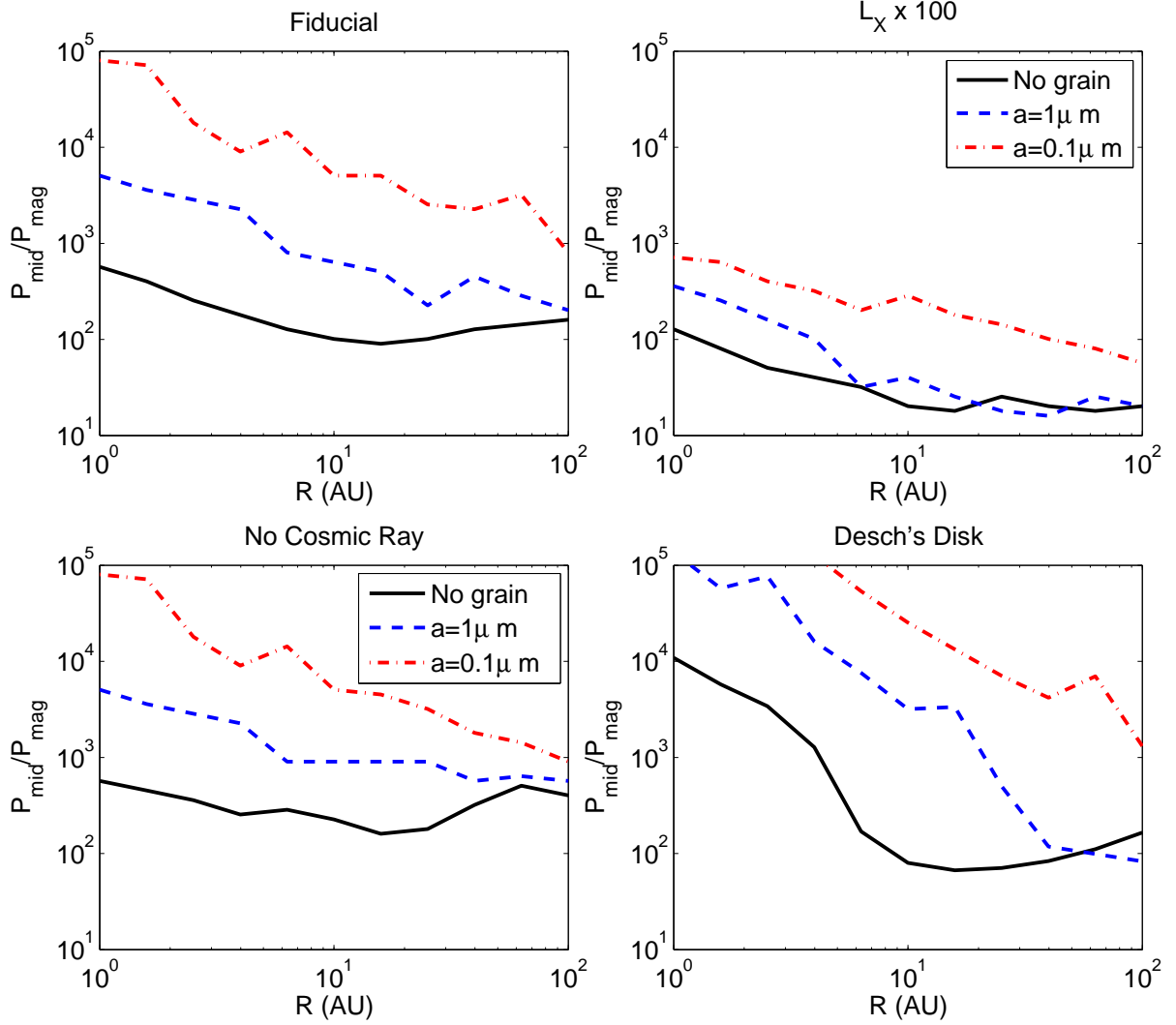


FIG. 5.— The ratio of midplane gas pressure to the optimal magnetic pressure at the active layer as a function of disk radius for our fiducial model (upper left): MMSN disk with cosmic ray and X-ray ionization, model with X-ray luminosity 100 times higher (upper right), model without cosmic-ray ionization (lower left) and model with the Desch’s disk (lower right). In each panel, we show results for calculations in the grain-free case (black solid), with well-mixed $1\mu\text{m}$ grains (blue dashed) and with $0.1\mu\text{m}$ grain (red dash-dotted).

chemical equilibrium. In particular, turbulent mixing of chemical species (especially electrons) can be compensated by the rapid recombination process. Additionally, we have updated the calculation of the sticking coefficient in electron-grain collisions where grain charge is taken into account. The electron sticking coefficient can deviate substantially from 1 which has a strong effect on the electron recombination rate and grain charge distribution, and should be treated with care.

Using the magnetic diffusion coefficients from the chemistry calculation, we estimate the location and extent of the regions in PPD models where the MRI can operate to drive disk accretion (i.e., the active layer). Our adopted criteria are based on the Ohmic Elsasser number Λ , where $\Lambda \gtrsim 1$ is required for the active layer as been shown by previous simulations (e.g., Turner et al. 2007; Ilgner & Nelson 2008), and the AD Elsasser number Am , where $\beta \gtrsim \beta_{\min}(Am)$ is required for sustained turbulence from the most recent study by BS11. We have ignored the Hall effect based on the study by Sano & Stone

(2002b), although the Hall regime is still yet to be more carefully explored with numerical simulations. Unlike most previous studies, we have considered the dependence of the diffusion coefficients (translated to the Elsasser number) on the magnetic field strength and show that the magnetic field strength can be a main limiting factor on the extent of the active layer because of AD. Our study shows that the conventional magnetic Reynolds number criterion with $Re_M \geq 100$ for the MRI to operate may substantially overestimates the column density of the MRI active layer in the presence of small grains.

We provide a general framework for estimating the upper limit of the MRI-driven accretion rate. Furthermore, we hypothesize that the MRI amplifies the magnetic field to maximize the accretion rate, from which we are able to make optimistic predictions on the accretion rate as well as the magnetic field strength in PPDs. Using this framework, we run a series of chemistry calculations with different model parameters to study the location and ex-

tent of the MRI active layers in PPDs, and to study the dependence of MRI-driven accretion rate \dot{M} on various parameters. The main results are summarized as follows.

1. Active layer always exists. Its upper boundary is set by AD, requiring the field strength not to be too strong. The lower boundary is generally determined by the Ohmic resistivity and the magnetic field strength, with the latter connected to the field strength in the upper boundary.
2. The predicted \dot{M} increases with disk radius in the inner disk where accretion is layered, and flattens or decreases with radius in the outer disk when the disk midplane becomes active. The transition radius depends on grain abundance, and is 4 – 10 AU in the grain-free case and above 50 AU in the presence of well-mixed sub-micron grains.
3. For our standard model, the predicted \dot{M} is a few times $10^{-9} M_{\odot} \text{ yr}^{-1}$ in the grain-free case, and is reduced by one to two orders of magnitude in the presence of sub-micron grains in the inner disk. Reduction of \dot{M} by grains is less significant in the outer disk.
4. The MRI-driven accretion rate is sensitive to the protostellar X-ray luminosity but insensitive to the deeper-penetrating cosmic-ray ionization rate. Extremely strong X-ray luminosity or additional strong ionization source with sufficient grain depletion is needed to achieve accretion rate of $\sim 10^{-7} M_{\odot} \text{ yr}^{-1}$.
5. In the inner disk where accretion is layered, the predicted \dot{M} increases with disk radius, but decreases with increasing disk surface density. This situation would lead to runaway mass pile-up in the inner disk if the MRI were the only mechanism for driving accretion in the inner region of PPDs.
6. The midplane gas pressure is generally a factor of 100 to 10^5 times higher than the predicted magnetic pressure in the active layer. The ratio is smaller for stronger ionization and higher for larger disk mass or in the presence of small grains. The predicted magnetic field strength in the outer disk is consistent with the non-detection of polarized emission resulting from grain alignment.

Our results place strong constraints on the effectiveness of the MRI-driven accretion in PPDs, especially for the inner disk with radius of about 1 – 10 AU where accretion is likely to be layered. There are two main difficulties concerning points 3 and 5 above: (a) The optimistically predicted accretion rate under standard model prescriptions is about one order of magnitude or more smaller than the typical observed value; (b) MRI-driven accretion would lead to the runaway pile-up of mass in the inner disk. The first difficulty might be alleviated by incorporating additional (but uncertain) ionization processes such as energetic protons from the protostellar activities. The second difficulty does not appear to be

easily reconciled, since external ionization sources always lead to layered accretion. The accumulation of mass may trigger the gravitational instability in the early phase of PPDs, which may further lead to outburst and episodic accretion as FU Ori-like events (Zhu et al. 2009). In later phases, mass accumulation may simply leads to very large surface density in the inner disk (Zhu et al. 2010). Since the inner disk ($\lesssim 10$ AU) is smaller than the resolution of the currently available sub-millimeter observations (Andrews et al. 2009), whether mass accumulation occurs may be distinguishable in future observations such as ALMA.

One possible resolution to the above difficulties may be achieved by a magnetized wind from the disk surface (Blandford & Payne 1982). The wind could be launched from the disk surface where the magnetic field is too strong for the MRI to operate, transporting angular momentum vertically by the Maxwell stress via ordered magnetic fields. Non-ideal MHD effects has been incorporated into wind models (Wardle & Koenigl 1993; Teitler 2011), and under favorable conditions, wind-driven accretion rate can become substantial (Königl et al. 2010; Salmeron et al. 2011). It has been proposed that disk wind may co-exist with the MRI (Salmeron et al. 2007), while they operate at different vertical locations. Current wind models for PPDs generally have a number of unconstrained free parameters, and further investigation (especially by numerical simulations) is needed to assess the effectiveness of disk wind on PPD accretions.

Our results are also applicable in the gas dynamics of transitional disks, where the MRI is likely to be responsible for driving accretion from the outer disk (Chiang & Murray-Clay 2007), with the inner gap / hole opened by multiple planets that guide the gas streams through (Perez-Becker & Chiang 2011a; Zhu et al. 2011). Our predicted accretion rate in the outer disk with $r \gtrsim 10$ AU is on the order of $10^{-9} M_{\odot} \text{ yr}^{-1}$, with relatively weak dependence on the dust content compared with the inner disk. The result is consistent with the range of observed accretion rate (Najita et al. 2007), thus MRI alone appears sufficient to account for the accretion rate in transitional disks. This conclusion can also be achieved with far UV ionization instead of X-rays (Perez-Becker & Chiang 2011b).

Our study of the MRI active layer in PPDs represents a first attempt to estimate the MRI-driven accretion rate that is based on the most up-to-date non-ideal MHD simulations. In the mean time, it is limited by the predictive power of the simulations themselves. In particular, the non-linear properties of the MRI in the Hall dominated regime is still unexplored. Moreover, the AD simulations by BS11 are unstratified, and whether their obtained criterion for sustained MRI turbulence holds remains to be verified in stratified simulations. In conclusion, our study calls for further progress in non-ideal MHD simulations, and in turn, more realistic criteria for sustained MRI turbulence can be easily incorporated into our general framework after future simulations.

X.-N.B. is grateful to Daniel Perez-Becker for valuable

comments to the original manuscript that lead to the corrections of an important code bug and some conclusions of the paper, to James Stone, Jeremy Goodman, Eugene Chiang and an anonymous referee for carefully reading the manuscript with helpful comments and suggestions, to Daniel Perez-Becker and Eugene Chiang for sharing their preprint on the importance of FUV ion-

ization, to Meredith Hughes, Geoffroy Lesur, Subu Mohanty, Raquel Salmeron, Neal Turner and Zhaohuan Zhu for useful discussions, and to Roy van Boekel and Greg Herczeg for organizing the Ringberg workshop for Transport Processes and Accretion in YSOs which led to improvements in this work.

APPENDIX

STICKING COEFFICIENT IN ELECTRON-GRAIN COLLISIONS AND GRAIN CHARGING

The collision of an electron with a grain particle does not necessarily lead to absorption because the electron has excess energy as it reaches the grain surface. The absorption probability P_e depends on the size of the grain a , grain charge Z , and the electron energy E . The sticking coefficient is defined as the absorption probability averaged over a thermal distribution of electron energies, which is a function of temperature T

$$s_e(a, Z, T) = \frac{\int_0^\infty \sigma(E) E e^{-E/kT} P_e(E) dE}{\int_0^\infty \sigma(E) E e^{-E/kT} dE}, \quad (\text{A1})$$

where $\sigma(E) = \sigma(a, Z, E)$ is the electron-grain cross section is given by Draine & Sutin (1987) (see their Section II). The task here is to calculate $P_e(E) = P_e(a, Z, E)$.

The sticking probability in the case of electron collision with neutral grains was derived in the Appendix B of Nishi et al. (1991). Below we generalize their derivation to include grain charge.

Let E_0 be the initial energy of the electron (at infinity), D be the depth of the potential well between the electron and the grain due to the electric polarization interaction (on the order of a few eV). The kinetic energy of the electron as it reaches the grain surface is therefore $E_0 + D + Ze^2/a$. In an inelastic collision with a surface atom/molecule (whose mass is M_s) of the grain, the upper limit of energy transfer is given by

$$\Delta E_u = \frac{4m_e}{M_s} (E_0 + \frac{Ze^2}{a} + D), \quad (\text{A2})$$

where m_e is the electron mass. From the phonon theory, the probability of inelastic collision electron collision α , and the averaged energy transfer in each inelastic collision δE , are given by (Umebayashi & Nakano 1980)

$$\alpha \approx \frac{3}{2} \frac{\Delta E_u}{kT_D}, \quad \delta E \approx \frac{kT_D}{18}, \quad (\text{A3})$$

where T_D is the Debye temperature of the lattice and is about 420K for graphite. The electron has to experience about l inelastic collisions on average before being truly absorbed, where l is given by

$$l\delta E > E_0 \geq (l-1)\delta E. \quad (\text{A4})$$

Between (say, the i th and the $(i+1)$ th) inelastic collisions, the electrons undergo elastic collisions with the grain and has a probability β_i to escape. Therefore, the absorption probability is given by (Umebayashi & Nakano 1980)

$$P_e = \prod_{i=0}^{l-1} \frac{1 - \beta_i}{1 - \beta_i + \beta_i/\alpha}. \quad (\text{A5})$$

The remaining task is to calculate β_i , corresponding to the electron escape probability when its total energy is $E_i = E_0 - i\delta E$. This is made convenient by considering energy conservation to write the radial energy of the electron as

$$E_r = E_i + \frac{Ze^2}{r} + \frac{e^2 a^3}{2r^2(r^2 - a^2)} - \left(\frac{a}{r}\right)^2 (E_i + \frac{Ze^2}{a} + D) \sin^2 \theta, \quad (\text{A6})$$

where the 2nd and 3rd terms represent the potential energy due to net charge and electric polarization, and the last term represents the transverse energy obtained from angular momentum conservation $L^2/2mr^2$, with θ being the angle between the velocity vector immediately after the elastic collision (scattering) and the radial direction. We see that E_r approaches infinity close to the grain surface due to electric polarization, and approaches E_i at infinity. If E_r becomes negative at some intermediate radius, it means that the electron can not travel beyond this radius and has to return to the grain surface for another collision. If E_r is positive at any r , the electron trajectory is open and will escape. Therefore, the purpose is to find the critical value of θ_{cr} , at which the function $E_r(r)$ touches the horizontal axis tangentially: $E_r = 0$ and $dE_r/dr = 0$. The latter condition can be more conveniently replaced by $d(r^2 E_r)/dr = 0$.

To proceed, we introduce dimensionless variables $x \equiv r/a$, $\Delta \equiv Da/e^2$ and $\epsilon_i = E_i a/e^2$, and obtain

$$\epsilon_i + \frac{1}{2x^2(x^2 - 1)} + \frac{Z}{x} = \frac{1}{x^2} (\epsilon_i + Z + \Delta) \sin^2 \theta_{\text{cr}}, \quad (\text{A7})$$

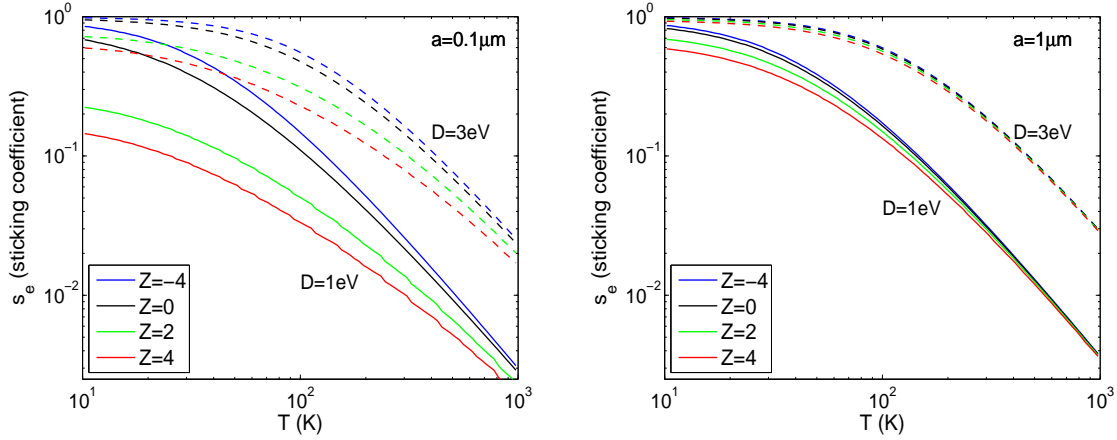


FIG. 6.— Electron sticking coefficient for $0.1\mu\text{m}$ (left) and $1\mu\text{m}$ (right) sized grains as a function of gas temperature. Two values of the binding energy $D=1\text{eV}$ (solid lines) and $D=3\text{eV}$ (dashed lines) are chosen. In each case, we show curves for different grain charges with $Z = -4$ (blue), $Z = 0$ (black), $Z = 2$ (green), and $Z = 4$ (red). Their sticking coefficients monotonically decrease as Z becomes larger and more positive. We adopt $D=1\text{eV}$ for all our chemistry calculations.

$$2x\epsilon_i + Z = \frac{x}{(x^2 - 1)^2}. \quad (\text{A8})$$

One can solve for x in equation (A8), which always has one solution for $x > 1$. We note that equation (A8) is equivalent to equation (2.10) of Draine & Sutin (1987) in the calculation of cross section, which is natural since electron escape is the inverse process of electron capture. Back substituting the solution of x to equation (A7) one obtains the critical angle θ_{cr} .

One caveat in the calculation is that the left hand side of equation (A7) can become negative when Z is negative and ϵ_i is small⁸. In fact, this expression is proportional to the electron-grain cross section (equation (2.8) of Draine & Sutin (1987)). This situation correspond to that a potential well with $E_r < 0$ always exist which prevents the electron from approaching the grain (in the case of electron capture), or escaping from the grain (in the case of we are interested here). If this occurs, we simply set the escaping probability $\beta_i = 0$ (or $\theta_{\text{cr}} = 0$). In fact, this means that after the i th collision, the electron is destined to be adsorbed even if its total energy $E_i > 0$.

Finally, by considering the process of elastic collisions as isotropic scattering, one obtains the absorption coefficient to be

$$\beta_i = \frac{1}{2\pi} \int_0^{\theta_{\text{cr}}} 2\pi \sin \theta d\theta = 1 - \cos \theta_{\text{cr}}. \quad (\text{A9})$$

As an example, we show the electron sticking coefficient for collisions with $0.1\mu\text{m}$ and $1\mu\text{m}$ grains in Figure 6. We see that s_e monotonically decrease with disk temperature and drops by about 2 orders of magnitude from 10K to 1000K. This is because the electron has more excess energy at higher temperature and has to undergo more inelastic and elastic collisions. Higher binding energy D raises the sticking coefficient, by reducing the critical angle θ_{cr} at each elastic collision. Our new result is that the sticking coefficient for negatively charged grains is in fact larger than that for positively charge grains⁹. This is reasonable because for negatively charged grains, the electron has been decelerated as it approaches the grain, thus bounces fewer times before being absorbed. Finally, the sticking coefficient is larger for larger grains. Meanwhile, the difference in the sticking probability for grains with different charged states is less for larger grains. Both are understandable since the electric potential due to grain charge at the grain surface reduced for large grains.

REFERENCES

- Acke, B. & van den Ancker, M. E. 2004, *A&A*, 426, 151
 Adams, F. C., Lada, C. J., & Shu, F. H. 1987, *ApJ*, 312, 788
 Andrews, S. M., Wilner, D. J., Hughes, A. M., Qi, C., & Dullemond, C. P. 2009, *ApJ*, 700, 1502
 —. 2010, *ApJ*, 723, 1241
 Armitage, P. J. 2010, *Astrophysics of Planet Formation*, ed. Armitage, P. J.
 —. 2011, *ARA&A*, arXiv:1011.1496
 Bai, X. & Stone, J. M. 2011, *ApJ*, in press (BS11, arXiv:1103.1380)
 Bai, X.-N. 2011, *ApJ*, accepted
 Bai, X.-N. & Goodman, J. 2009, *ApJ*, 701, 737 (BG09)
 Balbus, S. A. 2011, in *Physical Processes in Circumstellar Disks and Young Stars*, ed. P. Garcia, University of Chicago Press (arXiv:0906.0854)
 Balbus, S. A. & Hawley, J. F. 1991, *ApJ*, 376, 214
 Balbus, S. A. & Terquem, C. 2001, *ApJ*, 552, 235
 Blaes, O. M. & Balbus, S. A. 1994, *ApJ*, 421, 163
 Blandford, R. D. & Payne, D. G. 1982, *MNRAS*, 199, 883
 Calvet, N., D'Alessio, P., Hartmann, L., Wilner, D., Walsh, A., & Sitko, M. 2002, *ApJ*, 568, 1008
 Calvet, N., D'Alessio, P., Watson, D. M., Franco-Hernández, R., Furlan, E., Green, J., Sutter, P. M., Forrest, W. J., Hartmann, L., Uchida, K. I., Keller, L. D., Sargent, B., Najita, J., Herter, T. L., Barry, D. J., & Hall, P. 2005, *ApJ*, 630, L185

- Calvet, N. & Gullbring, E. 1998, *ApJ*, 509, 802
- Calvet, N., Muzerolle, J., Briceño, C., Hernández, J., Hartmann, L., Saucedo, J. L., & Gordon, K. D. 2004, *AJ*, 128, 1294
- Carballido, A., Bai, X., & Cuzzi, J. N. 2011, *MNRAS*, in press
- Chiang, E. & Murray-Clay, R. 2007, *Nature Physics*, 3, 604
- Chiang, E. & Youdin, A. N. 2010, *Annual Review of Earth and Planetary Sciences*, 38, 493
- Chiang, E. I. & Goldreich, P. 1997, *ApJ*, 490, 368
- Chiang, E. I., Joun, M. K., Creech-Eakman, M. J., Qi, C., Kessler, J. E., Blake, G. A., & van Dishoeck, E. F. 2001, *ApJ*, 547, 1077
- Cho, J. & Lazarian, A. 2007, *ApJ*, 669, 1085
- D'Alessio, P., Calvet, N., & Hartmann, L. 2001, *ApJ*, 553, 321
- D'Alessio, P., Calvet, N., Hartmann, L., Franco-Hernández, R., & Servín, H. 2006, *ApJ*, 638, 314
- D'Alessio, P., Canto, J., Calvet, N., & Lizano, S. 1998, *ApJ*, 500, 411
- Desch, S. J. 2004, *ApJ*, 608, 509
- . 2007, *ApJ*, 671, 878
- Draine, B. T. 2011, *Physics of the Interstellar and Intergalactic Medium* (Princeton and Oxford: Princeton University Press)
- Draine, B. T., Roberge, W. G., & Dalgarno, A. 1983, *ApJ*, 264, 485
- Draine, B. T. & Sutin, B. 1987, *ApJ*, 320, 803
- Dullemond, C. P. & Dominik, C. 2004, *A&A*, 417, 159
- Españolat, C., Calvet, N., D'Alessio, P., Bergin, E., Hartmann, L., Watson, D., Furlan, E., Najita, J., Forrest, W., McClure, M., Sargent, B., Bohac, C., & Harold, S. T. 2007, *ApJ*, 664, L111
- Fang, M., van Boekel, R., Wang, W., Carmona, A., Sicilia-Aguilar, A., & Henning, T. 2009, *A&A*, 504, 461
- Feigelson, E., Townsley, L., Güdel, M., & Stassun, K. 2007, *Protostars and Planets V*, 313
- Fleming, T. & Stone, J. M. 2003, *ApJ*, 585, 908
- Fleming, T. P., Stone, J. M., & Hawley, J. F. 2000, *ApJ*, 530, 464
- Fromang, S. & Nelson, R. P. 2006, *A&A*, 457, 343
- Fromang, S. & Papaloizou, J. 2006, *A&A*, 452, 751
- Fromang, S., Terquem, C., & Balbus, S. A. 2002, *MNRAS*, 329, 18
- Furlan, E., et al. 2006, *ApJS*, 165, 568
- Gammie, C. F. 1996, *ApJ*, 457, 355
- . 2001, *ApJ*, 553, 174
- Geers, V. C., Augereau, J., Pontoppidan, K. M., Dullemond, C. P., Visser, R., Kessler-Silacci, J. E., Evans, II, N. J., van Dishoeck, E. F., Blake, G. A., Boogert, A. C. A., Brown, J. M., Lahuis, F., & Merín, B. 2006, *A&A*, 459, 545
- Glassgold, A. E., Najita, J., & Igea, J. 2004, *ApJ*, 615, 972
- Gorti, U., & Hollenbach, D. 2004, *ApJ*, 613, 424
- Güdel, M., Briggs, K. R., Arzner, K., Audard, M., Bouvier, J., Feigelson, E. D., Franciosini, E., Glauser, A., Grosso, N., Micela, G., Monin, J., Montmerle, T., Padgett, D. L., Palla, F., Pillitteri, I., Rebull, L., Scelsi, L., Silva, B., Skinner, S. L., Stelzer, B., & Telleschi, A. 2007, *A&A*, 468, 353
- Gullbring, E., Calvet, N., Muzerolle, J., & Hartmann, L. 2000, *ApJ*, 544, 927
- Hartmann, L., Calvet, N., Gullbring, E., & D'Alessio, P. 1998, *ApJ*, 495, 385
- Hawley, J. F., Gammie, C. F., & Balbus, S. A. 1995, *ApJ*, 440, 742
- Hawley, J. F. & Stone, J. M. 1998, *ApJ*, 501, 758
- Hayashi, C. 1981, *Progress of Theoretical Physics Supplement*, 70, 35
- Heinemann, T., & Papaloizou, J. C. B. 2009a, *MNRAS*, 397, 52
- Heinemann, T., & Papaloizou, J. C. B. 2009b, *MNRAS*, 397, 64
- Herczeg, G. J. & Hillenbrand, L. A. 2008, *ApJ*, 681, 594
- Hillenbrand, L. A., Strom, S. E., Calvet, N., Merrill, K. M., Gatley, I., Makidon, R. B., Meyer, M. R., & Skrutskie, M. F. 1998, *AJ*, 116, 1816
- Hirose, S., & Turner, N. J. 2011, *ApJL*, 732, L30
- Hughes, A. M., Wilner, D. J., Andrews, S. M., Qi, C., & Hogerheijde, M. R. 2011, *ApJ*, 727, 85
- Hughes, A. M., Wilner, D. J., Calvet, N., D'Alessio, P., Claussen, M. J., & Hogerheijde, M. R. 2007, *ApJ*, 664, 536
- Hughes, A. M., Wilner, D. J., Cho, J., Marrone, D. P., Lazarian, A., Andrews, S. M., & Rao, R. 2009, *ApJ*, 704, 1204
- Igea, J. & Glassgold, A. E. 1999, *ApJ*, 518, 848
- Ilner, M. & Nelson, R. P. 2006, *A&A*, 445, 205
- . 2008, *A&A*, 483, 815
- Jin, L. 1996, *ApJ*, 457, 798
- Königl, A., Salmeron, R., & Wardle, M. 2010, *MNRAS*, 401, 479
- Kunz, M. W. & Balbus, S. A. 2004, *MNRAS*, 348, 355
- McCall, B. J., Huneycutt, A. J., Saykally, R. J., Geballe, T. R., Djuric, N., Dunn, G. H., Semaniak, J., Novotny, O., Al-Khalili, A., Ehlerding, A., Hellberg, F., Kalhori, S., Neau, A., Thomas, R., Österdahl, F., & Larsson, M. 2003, *Nature*, 422, 500
- Miller, K. A. & Stone, J. M. 2000, *ApJ*, 534, 398
- Muzerolle, J., Calvet, N., & Hartmann, L. 2001, *ApJ*, 550, 944
- Muzerolle, J., Hartmann, L., & Calvet, N. 1998, *AJ*, 116, 455
- Muzerolle, J., Luhman, K. L., Briceño, C., Hartmann, L., & Calvet, N. 2005, *ApJ*, 625, 906
- Najita, J. R., Strom, S. E., & Muzerolle, J. 2007, *MNRAS*, 378, 369
- Natta, A., Testi, L., & Randich, S. 2006, *A&A*, 452, 245
- Nishi, R., Nakano, T., & Umebayashi, T. 1991, *ApJ*, 368, 181
- Oishi, J. S. & Mac Low, M. 2009, *ApJ*, 704, 1239
- Okuzumi, S. 2009, *ApJ*, 698, 1122
- Oliveira, I., Pontoppidan, K. M., Merín, B., van Dishoeck, E. F., Lahuis, F., Geers, V. C., Jørgensen, J. K., Olofsson, J., Augereau, J., & Brown, J. M. 2010, *ApJ*, 714, 778
- Oppenheimer, M. & Dalgarno, A. 1974, *ApJ*, 192, 29
- Perez-Becker, D. & Chiang, E. 2011a, *ApJ*, 727, 2
- . 2011b, *ApJ*, 735, 8
- Preibisch, T., Kim, Y., Favata, F., Feigelson, E. D., Flaccomio, E., Getman, K., Micela, G., Sciortino, S., Stassun, K., Stelzer, B., & Zinnecker, H. 2005, *ApJS*, 160, 401
- Press, W. H., Teukolsky, S. A., Vetterling, W. T., & Flannery, B. P. 1992, *Numerical recipes in C. The art of scientific computing*, ed. Press, W. H., Teukolsky, S. A., Vetterling, W. T., & Flannery, B. P.
- Przygodda, F., van Boekel, R., Àbrahàm, P., Melnikov, S. Y., Waters, L. B. F. M., & Leinert, C. 2003, *A&A*, 412, L43
- Rafikov, R. R. 2009, *ApJ*, 704, 281
- Rice, W. K. M., Lodato, G., & Armitage, P. J. 2005, *MNRAS*, 364, L56
- Rice, W. K. M., Mayo, J. H., & Armitage, P. J. 2010, *MNRAS*, 402, 1740
- Salmeron, R., Königl, A., & Wardle, M. 2007, *MNRAS*, 375, 177
- Salmeron, R., Königl, A., & Wardle, M. 2011, *MNRAS*, 412, 1162
- Salmeron, R. & Wardle, M. 2003, *MNRAS*, 345, 992
- . 2005, *MNRAS*, 361, 45
- . 2008, *MNRAS*, 388, 1223
- Sano, T., Inutsuka, S., & Miyama, S. M. 1998, *ApJ*, 506, L57
- Sano, T., Miyama, S. M., Umebayashi, T., & Nakano, T. 2000, *ApJ*, 543, 486
- Sano, T. & Stone, J. M. 2002a, *ApJ*, 570, 314
- . 2002b, *ApJ*, 577, 534
- Semenov, D., Wiebe, D., & Henning, T. 2004, *A&A*, 417, 93
- Shakura, N. I. & Sunyaev, R. A. 1973, *A&A*, 24, 337
- Shu, F. 1991, *Physics of Astrophysics, Vol. II: Gas Dynamics*, ed. Shu, F. (University Science Books)
- Sicilia-Aguilar, A., Hartmann, L., Calvet, N., Megeath, S. T., Muzerolle, J., Allen, L., D'Alessio, P., Merín, B., Stauffer, J., Young, E., & Lada, C. 2006, *ApJ*, 638, 897
- Sicilia-Aguilar, A., Hartmann, L. W., Hernández, J., Briceño, C., & Calvet, N. 2005, *AJ*, 130, 188
- Sicilia-Aguilar, A., Henning, T., & Hartmann, L. W. 2010, *ApJ*, 710, 597
- Simon, J. B., Hawley, J. F., & Beckwith, K. 2011, *ApJ*, 730, 94
- Stelzer, B., Flaccomio, E., Briggs, K., Micela, G., Scelsi, L., Audard, M., Pillitteri, I., & Güdel, M. 2007, *A&A*, 468, 463
- Stone, J. M., Hawley, J. F., Gammie, C. F., & Balbus, S. A. 1996, *ApJ*, 463, 656
- Teitler, S. 2011, *ApJ*, 733, 57
- Tsiganis, K., Gomes, R., Morbidelli, A., & Levison, H. F. 2005, *Nature*, 435, 459
- Turner, N. J., Willacy, K., Bryden, G., & Yorke, H. W. 2006, *ApJ*, 639, 1218
- Turner, N. J. & Drake, J. F. 2009, *ApJ*, 703, 2152
- Turner, N. J. & Sano, T. 2008, *ApJ*, 679, L131
- Turner, N. J., Sano, T., & Dziourkevitch, N. 2007, *ApJ*, 659, 729
- Umebayashi, T. & Nakano, T. 1980, *PASJ*, 32, 405
- . 1981, *PASJ*, 33, 617
- . 2009, *ApJ*, 690, 69
- van Boekel, R., Min, M., Waters, L. B. F. M., de Koter, A., Dominik, C., van den Ancker, M. E., & Bouwman, J. 2005, *A&A*, 437, 189

- van Boekel, R., Waters, L. B. F. M., Dominik, C., Bouwman, J., de Koter, A., Dullemond, C. P., & Paresce, F. 2003, *A&A*, 400, L21
- Vasyunin, A. I., Semenov, D., Henning, T., Wakelam, V., Herbst, E., & Sobolev, A. M. 2008, *ApJ*, 672, 629
- Vorobyov, E. I. & Basu, S. 2007, *MNRAS*, 381, 1009
- Wardle, M. 1999, *MNRAS*, 307, 849
- . 2007, *Ap&SS*, 311, 35
- Wardle, M. & Koenigl, A. 1993, *ApJ*, 410, 218
- Wardle, M., & Salmeron, R. 2011, *MNRAS*, submitted (arXiv:1103.3562)
- Watson, D. M., et al. 2009, *ApJS*, 180, 84
- Weidenschilling, S. J. 1977, *Ap&SS*, 51, 153
- Wolk, S. J., Harnden, Jr., F. R., Flaccomio, E., Micela, G., Favata, F., Shang, H., & Feigelson, E. D. 2005, *ApJS*, 160, 423
- Woodall, J., Agúndez, M., Markwick-Kemper, A. J., & Millar, T. J. 2007, *A&A*, 466, 1197
- Zhu, Z., Hartmann, L., Gammie, C., & Mckinney, J. C. 2009, *ApJ*, 701, 620
- Zhu, Z., Hartmann, L., & Gammie, C. 2010, *ApJ*, 713, 1143
- Zhu, Z., Nelson, R. P., Hartmann, L., Espaillat, C., & Calvet, N. 2011, *ApJ*, 729, 47